

[Click here to view linked References](#)

1 **Experimental calibration of vanadium partitioning and stable isotope** 2 **fractionation between hydrous granitic melt and magnetite at 800°C and 0.5 GPa**

3 Paolo A. Sossi^{1*}, Julie Prytulak² & Hugh St.C. O'Neill¹

4 ¹ Research School of Earth Sciences, Australian National University, Canberra, 2601, ACT, Australia

5 ² Department of Earth Science and Engineering, Imperial College London, SW7 2AZ, UK

6 *Corresponding author. Present address: Institut de Physique du Globe de Paris, Sorbonne Paris Cité, Université
7 Paris Diderot, CNRS, F-75005 Paris, France. *E-mail address:* sossi@ipgp.fr

8 **Abstract**

9 Vanadium has multiple oxidation states in silicate melts and minerals, a property that also promotes
10 fractionation of its isotopes. As a result, vanadium isotopes vary during magmatic differentiation, and
11 can be powerful indicators of redox processes at high temperatures if their partitioning behaviour can
12 be determined. In order to quantify the isotope fractionation factor between magnetite and melt, piston
13 cylinder experiments were performed in which magnetite and a hydrous, haplogranitic melt were
14 equilibrated at 800°C and 0.5 GPa over a range of oxygen fugacities (fO_2), bracketing those of
15 terrestrial magmas. Magnetite is systematically ⁵¹V-depleted with respect to the coexisting melt, a
16 tendency ascribed to the predominantly VI-fold V³⁺ in magnetite, and a mixture of IV- and VI-fold
17 V⁵⁺ and V⁴⁺ in the melt. The magnitude of the fractionation factor systematically increases with
18 increasing $\log fO_2$ relative to the Fayalite-Magnetite-Quartz buffer (FMQ), from $\Delta^{51}V_{\text{mag-gl}} = -$
19 $0.63 \pm 0.09\text{‰}$ at FMQ-1 to $-0.92 \pm 0.11\text{‰}$ (SD) at \approx FMQ+5. These first mineral-melt measurements of
20 V isotope fractionation factors underline the importance of both oxidation state and co-ordination
21 environment in controlling isotopic fractionation. The fractionation factors determined experimentally
22 are in excellent agreement with those needed to explain natural isotope variations in magmatic suites.
23 Further, these experiments provide a useful framework in which to interpret vanadium isotope
24 variations in natural rocks and magnetites, and may be used as a potential fingerprint the redox state
25 of the magma from which they crystallise.

26 **Keywords:** Redox, Magnetite, Magma, Vanadium, Stable Isotope Fractionation, Equilibrium

27 **Word Count = 7,287; Figures = 6; Tables = 8**

28

29 Introduction

30 Among the polyvalent elements, vanadium is particularly unique in that it exists in five oxidation
31 states, V^0 , V^{2+} , V^{3+} , V^{4+} and V^{5+} . This wide range of valence states brackets the oxygen fugacities
32 (fO_2) of natural rocks, and thus elemental partitioning of V has been employed as a redox indicator
33 (e.g., Canil 1997; Lee et al. 2005; Mallmann and O'Neill, 2009; 2013).

34 Pure magnetite has an inverse spinel structure at room temperature, with the formula
35 $^{IV}(Fe^{3+})^{VI}(Fe^{2+}Fe^{3+})O_4$, however, it tends to the random, normal distribution at $\approx 1400^\circ C$ (Wu and
36 Mason, 1981). In the absence of titanium, the Fe^{3+}/Fe^{2+} ratio of two in magnetite is imposed by its
37 stoichiometry, making it independent of fO_2 of the melt from which it crystallises. The high
38 octahedral site preference energy of V^{3+} makes its incorporation favourable into magnetite by the
39 reaction $VO_{1.5} + FeO = FeV_2O_4$, which is a normal spinel. Together, the Fe^{3+}/Fe^{2+} and V^{4+}/V^{3+} pairs
40 undergo electron exchange that results in the stabilisation of all four species at high temperatures,
41 leading to considerable configurational entropy and negative deviations from ideality in Fe_3O_4 -
42 FeV_2O_4 solid solutions (Petric and Jacob, 1982; O'Neill and Navrotsky, 1984). This phenomenon
43 renders V^{3+} highly compatible in magnetite, and the V^{4+}/V^{3+} ratio is also independent of fO_2 at a given
44 temperature and pressure.

45 Due to the important role magnetite plays in evolving magmas, vanadium partition coefficients are
46 well-characterised over a range of fO_2 (e.g., Canil and Fedourtchuk, 2001; Righter et al., 2006a;
47 Toplis and Corgne, 2002, Mallmann & O'Neill, 2009), though, until recently, few at melt
48 compositions relevant to the silicic magmas from which they predominantly crystallise. Arató and
49 Audétat (2017) measured the partitioning of V between magnetite and silicic melts with varying
50 Alumina-Saturation Indices (ASI), molar $Al_2O_3/(CaO+Na_2O+K_2O)$, between $800^\circ C$ and $1000^\circ C$,
51 observing that V becomes more compatible at lower temperatures and higher ASI. A similar
52 dependence was observed by Sievwright et al. (2017), who further showed that V substitution into
53 titanomagnetite follows that of Ti. In both cases, the logarithm of the partition coefficient of V into
54 magnetite compared with $\log fO_2$ resulted in a slope of -0.5, implying that V is largely trivalent in
55 magnetite, whereas V^{5+} prevails in the silicate liquid.

56 Stable V isotopes can now be determined to a precision high enough to be applied to geological
57 problems (e.g., Nielsen et al., 2011; Prytulak et al., 2011; Wu et al., 2016). The nascent dataset,
58 including peridotites, mafic magmas and meteorites (Prytulak et al., 2011; Prytulak et al. 2013,
59 Nielsen et al. 2014; Wu et al., 2016; Prytulak et al. 2017; Schuth et al. 2017; Sossi et al. 2017) reveals
60 analytically resolvable V isotope fractionations at high temperatures. The strong dependence of V
61 partitioning on fO_2 makes it tempting to interpret isotope variations in terms of variable oxygen
62 fugacity. Even at igneous temperatures, variable bond strength gives rise to stable isotope

63 fractionation, with heavier isotopes preferred in stronger bonding environments (e.g. Urey, 1947;
64 Schauble, 2004). Whilst the valence of an element plays a role in determining bond strength, the co-
65 ordination environment is also key (e.g., Sossi and O'Neill, 2017).

66 Vanadium isotopes, during the early phase of crystallisation dominated by Fe-Mg silicates and
67 plagioclase, are invariant in natural magmatic systems from island arc (Marianas) and intraplate
68 (Hekla, Iceland) environments (Prytulak et al., 2017), and V is mildly incompatible. However, upon
69 Fe-Ti oxide saturation in dacitic compositions, the V isotope composition of the remaining melt
70 increases to 2‰ higher than in mafic compositions. This phenomenon is a result of Rayleigh
71 distillation and a magnetite-melt fractionation factor of $\approx -0.5\%$ at around 1000-1050°C (Prytulak et
72 al., 2017). At the resolution of their measurements, no co-variation of the fractionation factor with the
73 fO_2 of the magma (FMQ for Hekla, FMQ+2 for Marianas) is apparent. As such, both the differing co-
74 ordination and V oxidation state inferred between magnetite ($^{VI}V^{3+}$) and melt ($^{IV-VI}V^{4+}$ and $^{IV}V^{5+}$) are
75 required to drive isotopic fractionation, but it is problematic to deconvolve these parameters from one
76 another in natural rocks. Thus, before natural variations in stable vanadium isotopes can be
77 interpreted in the context of fO_2 , the response of isotope fractionation to oxygen fugacity and other
78 physicochemical variables must be systematically examined.

79 This contribution presents the first experimental investigation of stable vanadium isotope
80 fractionation. Stable V isotope fractionation factors are determined between hydrous, granitic melts
81 and magnetite equilibrated in a piston cylinder assembly at 800°C and 0.5 GPa as a function of
82 oxygen fugacity. These conditions were chosen to maximise the isotopic fractionation factor whilst
83 still resembling natural systems. Elemental partitioning between the two phases is fit using a
84 thermodynamic model that yields estimates for Fe^{2+}/Fe^{3+} and $V^{3+}/V^{4+}/V^{5+}$ ratios in the melt. With this
85 information, V isotope fractionation between magnetite and melt is modelled using the bond valence
86 model. It is shown that V isotope fractionation between experimental magnetite and melt is sensitive
87 to both co-ordination environment and oxygen fugacity, and thus potentially useful in deciphering
88 redox conditions during igneous processes and for fingerprinting the origin of magnetite with
89 differing petrogenetic histories.

90 **Methods & Rationale**

92 **Experimental Petrology**

93 Magnetite has several attributes that make it an attractive target for the experimental investigation of
94 vanadium stable isotope fractionation. These include the ubiquity of magnetite in igneous systems, the
95 importance of the mineral in understanding the genesis of arc magmas (e.g., Jenner et al., 2010), the
96 high compatibility of vanadium in magnetite (except under very oxidising conditions; Toplis and

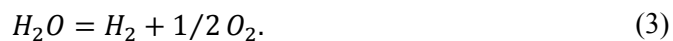
97 Corgne, 2002), the growing body of work using magnetite chemistry for economic tracing (e.g.,
 98 Boutroy et al. 2014; Dare et al. 2014; Canil et al. 2016) and its magnetic properties, which aids phase
 99 separation of experimental charges. Importantly, incorporation of V^{3+} in magnetite is favoured
 100 stoichiometrically over other oxidation states, so that its speciation is independent of oxygen fugacity
 101 (O'Neill and Navrotsky, 1984) hence isotopic variations can be ascribed almost solely to changes in V
 102 bonding environment in the melt.

103 Whilst analytically resolvable variations in vanadium isotopes have been demonstrated in high
 104 temperature materials (Prytulak et al., 2011; 2013; Nielsen et al., 2014; Prytulak et al. 2017; Schuth et
 105 al. 2017; Sossi et al. 2017), the magnitude of fractionation is $\approx 1\%$. Thus, the experiments presented
 106 herein were devised to maximise potential isotope fractionation, rather than replicate natural systems.
 107 Temperature affects stable isotope fractionation proportional to $1/T^2$ (Urey, 1947). In attempting to
 108 minimise temperatures (and therefore maximise isotope fractionation) required for a liquid melt to
 109 exist, a haplogranitic melt was chosen (Table 1). To further decrease the liquidus temperature and
 110 promote equilibration, water was added as a flux. By interpolation of H_2O contents at saturation in
 111 different haplogranite compositions (Holtz et al., 2001), water saturation is calculated to be 10.2 wt.
 112 % at $800^\circ C$ and 0.5 GPa for the haplogranite used in this work (Table 1). In order to prevent the
 113 formation of a fluid phase, which could complex V, 9 wt. % water was added, keeping the melt just
 114 below the saturation point. Vanadium was added at 4 wt. % of the total mixture.

115 In order to control fO_2 in piston cylinder experiments, the double capsule method (Eugster, 1957;
 116 Woodland and O'Neill, 1997; Matjuschkin et al., 2015) was employed. This technique is predicated
 117 on the rapid diffusion of hydrogen and use of H_2O as an oxygen buffering agent, where the $\frac{f_{O_2}}{f_{H_2}}$ ratio is
 118 controlled by the redox potential of the E^0/E^{x+} pair. More reducing metals will be in equilibrium with
 119 a vapour phase that has a lower H_2O/H_2 ratio.



120 Then, subtracting equation (2) from (1) gives:



121 Hydrogen diffusion proceeds from the outer reservoir into the inner capsule, which is fashioned from
 122 a 0.2 mm wall thickness, 3.5 mm external diameter $Ag_{75}Pd_{25}$, rather than the pure Ag, 6.3 mm
 123 external diameter outer capsule. The Silver-Palladium capsule is less prone to Fe loss compared to Pt
 124 (Muan, 1963), and offers comparable H_2 permeability that is an order of magnitude greater than that
 125 of pure silver at $800^\circ C$ (Chou, 1986). At equilibrium, equation (3) can be expressed as:

$$\log f_{O_2} = 2 \log a_{H_2O} - 2 \log f_{H_2} + 2 \log K . \quad (4)$$

1
2 126 If the hydrogen pressures are equivalent in the inner and outer capsules, f_{O_2} should be equivalent in
3 127 both. However, in the experiments designed here, H_2O is slightly undersaturated in the inner capsule,
4
5 128 yielding an $a_{H_2O} < 1$. Therefore, the oxygen fugacity in the inner capsule is given by:

$$\log f_{O_2}^{inner} = \log f_{O_2}^{outer} + 2 \log a_{H_2O} . \quad (5)$$

6
7
8
9
10 129 Here, it is assumed that the activity of water, $a_{H_2O} = f_{H_2O}/f_{H_2O}^o$, where f^o is the fugacity at saturation
11 130 (= 1). Mole fractions of water dissolved in granitic melts were calculated as a function of composition
12
13 131 at 800°C according to Behrens and Jantos (2000).

14
15 132 The solid-solid buffers chosen span the range of typical terrestrial oxygen fugacities found in granitic
16 133 rocks (*e.g.*, Carmichael, 1991). At 800°C, they become more oxidising from Co-CoO < NNO < Re-
17 134 ReO₂ < HM, corresponding to FMQ-0.78, FMQ+0.81, FMQ+2.87 and FMQ+5.07, respectively. As
18
19 135 the intrinsic f_{O_2} of piston cylinder charges are around FMQ (Boettcher et al., 1973; Medard et al.,
20 136 2008), the molar ratios of the metal-metal oxide mixtures were set such that the more unstable
21
22 137 component was in excess. For Co:CoO, 75:25, Ni:NiO = 50:50, Re:ReO₂ = 67:33 and 75:25
23
24 138 Hematite:Magnetite. The presence of water and both phases was verified after the experiment by
25
26 139 XRD, ensuring that the oxygen fugacity was buffered by the two-phase assemblage, to an uncertainty
27
28 140 of ± 0.3 log units (Matjuschkin et al., 2015).

29
30
31 141 To verify the reliability of the more complex piston cylinder experiments, a simpler experiment was
32 142 run in a 1 atm vertical gas-mixing furnace. A sodium silicate melt composition in the system Na₂O-
33 143 SiO₂-Fe₂O₃ was devised (Bowen et al., 1930) to remain super-solidus at 800°C and fluid-absent
34
35 144 conditions. The oxides were added in the proportions 23:37:38 (Table 1), yielding a composition with
36
37 145 a liquidus temperature around 900°C. Above the hematite-magnetite buffer, liquids of this
38
39 146 composition crystallise only hematite down to the ternary eutectic temperature of 809°C. To this mix,
40
41 147 2 wt. % V₂O₃ was added, and the experiment was run in an open Ag crucible suspended from an
42
43 148 alumina loop by Pt wire at FMQ-1. Oxygen fugacity was set by a CO-CO₂ gas mixture, with which
44
45 149 the melt interacted at 800°C to crystallise magnetite. A summary of experimental conditions, run
46
47 150 times and weights can be found in Table 2.

48
49 151 The experiments were finely crushed, and magnetite was separated gravitationally by settling in
50
51 152 acetone, where the recovered material was subjected to the same treatment several times, resulting in
52
53 153 near-pure glass fractions. Experiments with coarser-grained magnetite were also separated
54
55 154 magnetically from the silicate glass. The sodium silicate composition has the added benefit of being
56
57 155 soluble in water (Fuchs, 1825), whereas magnetite was dissolved in 6M HCl.

58 156 **Electron Microprobe**

157 Major element analyses of the experimentally-grown phases were performed on a Cameca SX100 at
158 the Research School of Earth Sciences (RSES), Australian National University (RSES, ANU) using
159 wavelength dispersive spectroscopy (WDS). Spectrometers were initially calibrated for peak position
160 and intensity on in-house natural mineral standards, and three Smithsonian National History Museum
161 internal standards, San Carlos Olivine, Kakanui Augite and Tiebaghi Chromite (Jarosewich et al.,
162 1980) corrected for in-run drift. Beam conditions were set at 15 kV and 20 nA for a 1 μm focused
163 spot, increased to 20 μm broad beam for glasses. Peak counting times varied depending on the
164 element; Si, Al and Mg were run on TAP with a 10 s count time each while Na was analysed for 20s
165 on the same crystal. Calcium and K were run on PET for 10 s and 20 s, respectively. Iron was
166 analysed for 10 s on the more sensitive LLIF crystal, together with the V $K\alpha$ peak (as opposed to $K\beta$
167 which is less intense and has interferences from Cr and especially Ti) with a count time of 120 s on
168 two spectrometers, yielding an estimated detection limit of 40 ppm. Reported glass and mineral
169 compositions are an average of between 5 – 10 points.

170 **Isotope Geochemistry**

171

172 *Analytical Considerations*

173 Vanadium has two stable isotopes, whose abundances are highly skewed between ^{51}V (99.76%) and
174 ^{50}V (0.24%). The existence of only two stable isotopes precludes the use of a double spiking
175 technique to correct for mass fractionation. Mass fractionation of stable isotopes may be induced
176 during ion exchange chromatography due to incomplete elution (see Anbar et al., 2000; Chapman et
177 al., 2006; Sossi et al., 2015). Therefore, quantitative (100%) recovery of V is required. In addition, the
178 purification of V is further complicated by the isobaric interferences of ^{50}Cr and ^{50}Ti (4.31% and
179 5.34%, respectively) on the minor isotope, ^{50}V . As such, the accurate and precise measurement of the
180 isotopes of vanadium also necessitates near-quantitative removal of Cr and Ti (Nielsen et al., 2011;
181 Prytulak et al., 2011).

182 *Ion Exchange Chromatography*

183 Samples, including separated experimental charges and United States Geological Survey (USGS)
184 reference materials were dissolved in HCl-HF- HNO_3 in the ratio 1:0.5:0.2 for 48 hours at 140°C in
185 sealed Teflon vials. The USGS reference material PCC-1 is a Cr-spinel rich harzburgite, that was
186 digested in an oven in pressurised, sealed Teflon bombs in a 3:1 mixture of concentrated HNO_3 :HF
187 for 6 days at 210°C. PCC-1 was then evaporated under concentrated HNO_3 .

188 The procedure of Nielsen et al. (2011) was followed in order to satisfy the requirements of 1)
189 complete recovery of V and 2) quantitative removal of Cr and Ti. All work was carried out in a
190 laminar flow hood at RSES, ANU.

191 *Mass Spectrometry*

192 Analyses were performed on a ThermoFinnigan Neptune Plus MC-ICP-MS at RSES, ANU. Stable
193 vanadium isotopes are reported using standard delta notation, relative to the Oxford Alfa Aesar V
194 solution standard (AA), defined as 0‰ (Nielsen et al., 2011; Prytulak et al., 2011).

$$\delta^{51}V_{AA} (\text{‰}) = \left(\frac{(^{51}V/^{50}V)_{\text{sample}}}{(^{51}V/^{50}V)_{AA}} - 1 \right) \times 1000 \quad (6)$$

196 The Neptune Plus at ANU is equipped with $10^{10} \Omega$ and $10^{11} \Omega$ resistors. The major isotope, ^{51}V was
197 measured on a $10^{10} \Omega$ resistor to mute the overwhelming signal whilst still achieving statistically
198 meaningful counts on ^{50}V . The measurement protocol followed that outlined in Sossi et al. (2017).
199 Briefly, sample solutions and standards were analysed in 0.3M HNO₃ at a concentration of 4 ppm, in
200 Low Resolution (LR) mode, using H-cones. Each analysis comprised of 45 cycles of 4.194 s each. An
201 instrumental baseline is implemented before each analysis, in addition to a blank subtraction
202 performed every bracketing standard. The cup configuration is given in Table 3, and allows for
203 collection of the Ti and Cr masses, a requirement for application of the interference correction on ^{50}V .
204 Interference and mass bias corrections were applied using the exponential law to both the samples and
205 standard. Uncertainties are reported as standard deviations throughout.

206 **Results**

208 **Petrography**

209 A back-scattered electron image of a representative section of the Re-ReO₂ experiment is shown in
210 Figure 1. All experimental runs produced magnetite and glass. The two phases are present in 1:1
211 proportions, reflecting the ratio of magnetite:haplogranite in the starting mixture (Table 1). Magnetite
212 predominantly occurs as small (5-20 μm) euhedral crystals that often form glomeroporphyritic
213 clusters of $\approx 100\mu\text{m}$. A small fraction (5-10%) of the magnetite occurs as larger, embayed phenocrysts
214 of up to 50 μm in length, whose growth may have resulted from pressure fluctuations over the course
215 of the experiments. The glass is vitric and unvesiculated. Both magnetite and glass phases are
216 homogeneous, with no chemical zoning evident with proximity to the capsule walls, within phases or
217 where both are in contact.

219 **Major and Minor element compositions**

220 Compositions of silicate glass and magnetite are reported in Table 4. Water contents, calculated by
221 difference of the total to 100 wt. %, range from 6.89 wt. % (HM) to 9.45 wt. % (NNO), likely
222 reflecting the imprecision in adding 9 μL of water to the experimental charge. Importantly, these are
223 all lower than the theoretical water saturation content of the granitic melt (Holtz et al., 2001). With

224 respect to the initial starting composition, the alkali contents are depleted, ranging from a combined
225 total of 6.25 to 6.79 wt. % on an anhydrous basis, compared to 9.48 wt. % in the starting mix. Their
226 decrease is at the expense of Al_2O_3 , $\text{FeO}^{(\text{T})}$ and V_2O_3 , with the latter two showing trends in their
227 concentration with $f\text{O}_2$ (Fig. 2a,b). As oxygen fugacity increases, iron shows a parabolic decrease
228 from 3.35 wt. % at Co-CoO to 1.57 wt. % at HM (Fig. 2a). The opposite dependence is observed for
229 V (Fig. 2b), with higher concentrations under more oxidised conditions (1443 ± 61 ppm at HM),
230 compared to 268 ± 49 ppm at Co-CoO. Over the same range in oxygen fugacity, magnetite
231 compositions remain comparatively constant, with $6.89 < \text{V}_2\text{O}_3$ (wt. %) < 8.39 and $84.40 < \text{FeO}^{(\text{T})}$ (wt.
232 %) < 86.23 , and, when re-calculated for 3 cations/4 oxygens, correspond to coulsonite components
233 (X_{coul}) of 0.11 to 0.13 (Table 4). In the 1 atm experiment at FMQ-1, V is incompatible in magnetite,
234 with $\text{V}_2\text{O}_3 = 0.33 \pm 0.10$ wt. % ($X_{\text{coul}} = 0.005$), compared to 2.67 ± 0.03 wt. % in the melt.

235 **V isotopic Compositions of solution standards and USGS Reference Materials**

236 The first assessment of the long-term reproducibility of BDH is $\delta^{51}\text{V}_{\text{AA}} = -1.19 \pm 0.08\text{‰}$ ($n \approx 1000$;
237 Nielsen et al., 2011). Later studies are in excellent agreement with this value (Wu et al., 2016: $\delta^{51}\text{V}_{\text{AA}}$
238 $= -1.23 \pm 0.04\text{‰}$ ($n=197$), Schuth et al., 2017; $\delta^{51}\text{V}_{\text{AA}} = -1.22 \pm 0.04\text{‰}$ ($n=10$), and Sossi et al. (2017), -
239 $1.10 \pm 0.08\text{‰}$, ($n=5$). Continual measurement of BDH at RSES, ANU over the time period of unknown
240 samples measured in this study yields $-1.13 \pm 0.06\text{‰}$ ($n = 28$). This consistency attests to the capability
241 of measuring V isotopes in a pure V solution using the ANU analytical protocol. These values
242 compares well with the column-processed V_2O_3 starting material (also BDH) and BDH solution,
243 which give $-1.17 \pm 0.16\text{‰}$ and $-1.22 \pm 0.12\text{‰}$, respectively. In addition, USGS reference materials were
244 analysed to test the reproducibility and accuracy of the wet chemistry (sample dissolution and ion
245 exchange purification). Standard data for USGS reference materials is in agreement with literature
246 data (Table 5). In fact, BIR-1 agrees well in all laboratories that measured this standard, even though
247 different combinations of medium and low resolution, wet and dry plasma, 10^9 , 10^{10} , 10^{12} resistors
248 and different instruments (the Neptune and the Nu) were employed (Table 5). The same is true of
249 BCR-2, with the exception of the heavier value of $-0.78 \pm 0.04\text{‰}$ reported by Wu et al. (2016). The
250 stability of V isotope compositions processed using ion exchange chromatography across numerous
251 labs employing diverse analytical protocols testifies to the robustness of the values reported herein.

252 **V isotopic composition of magnetite and glass in experimental charges**

253 Vanadium isotope compositions of separated magnetite and glass are listed in Table 6. The V isotope
254 composition of the starting material (BDH) is $\delta^{51}\text{V}_{\text{AA}} = -1.19 \pm 0.08\text{‰}$ (Nielsen et al., 2011). In most
255 cases, measured magnetite compositions are marginally heavier than this value, from $-1.35 \pm 0.06\text{‰}$ to
256 $-1.48 \pm 0.07\text{‰}$, while magnetite in the NNO experiment has $-1.79 \pm 0.06\text{‰}$. The glass phase is always
257 systematically heavier than its coexisting magnetite, between $-0.88 \pm 0.09\text{‰}$ to $-1.16 \pm 0.09\text{‰}$, again

258 close to the starting composition, but clearly resolved from magnetite. Measured isotope differences
259 between magnetite and glass vary between $-0.32 \pm 0.11\%$ and $-0.70 \pm 0.08\%$.

260 Discussion

261

262 Correcting for contamination and open-system behaviour of V in experiments

263 The time required to achieve isotopic equilibrium may be tested by performing a time-series, whereby
264 all other variables are held constant aside from the run duration. Here, two experiments were run for
265 three days (Co-CoO and HM), whereas the Re-ReO₂ and NNO experiments were run for 7 and 14
266 days, respectively. The coherence of all four experiments with one another in chemical and isotopic
267 trends (Fig. 1a,b, Fig. 2) suggests attainment of isotopic equilibrium with run times longer than three
268 days. Additionally, as magnetite was grown from oxide powders rather than equilibrated, grain
269 growth should occur in equilibrium with the melt.

270 Diffusion rates for V⁴⁺, presumed to be the most abundant V species in the melt (*e.g.* Toplis and
271 Corgne, 2002) are estimated with the empirical, viscosity-based model of Mungall (2002). At 1073K
272 and 5 kb, and an average XH₂O = 23.1 (mol. %) the calculated $\log \eta = 3.7$ (Pa.s; Ardia et al., 2008),
273 gives rise to V diffusivity of 3.0×10^{-10} cm²/s. For an inner capsule radius of 1.5 mm, equilibration
274 times over the length scale of the capsule are 8.7 days (3 days gives equilibration length scales of 0.9
275 mm). These timescales are sufficient for equilibration over the length scale of melt-magnetite
276 equilibrium, which occurs over 100-200 μ m (Fig. 1).

277 Despite evidence for equilibrium, open system behaviour, resulting from the loss of vanadium from
278 either the melt or magnetite, must be evaluated. The most likely culprits are a) complexation of V by a
279 fluid phase and b) alloying of V with the ⁷⁵Ag-²⁵Pd capsule. The recovered charges are unvesiculated
280 (Fig. 1) and have lower water contents than required for fluid saturation, obviating loss of V in a fluid
281 phase. While V is immiscible in Ag (Smith, 1989), it readily forms alloys with Pd (Massalski, 1990).
282 However, the low temperatures, high *f*O₂ and high Ag proportion in the Ag-Pd alloy minimise V loss
283 to the inner capsule. The degree to which V loss affected each experiment may be quantified by mass
284 balance. Re-constructed total V₂O₃ contents, considering that 50% of the mix is comprised of
285 magnetite (differential dissolution of magnetite into melt at different *f*O₂ has no effect on the
286 calculated proportions), are given in Table 6. With the exception of the NNO run (3.41 ± 0.16 wt. %)
287 all experiments are within uncertainty of the 4 wt. % in the starting mix. The 1 atm experiment
288 yielded 1.82 ± 0.06 wt. % V₂O₃, compared with the 2 wt. % in the starting mix, and it is noteworthy
289 that the magnitude of the V isotope fractionation factor in this experiment is consistent with the high
290 pressure experiments. Therefore, with the exception of the NNO run, which lost <15% V, the
291 experiments acted as closed systems with respect to V.

292 To quantify the purity of the separated glass and magnetite fractions, V concentrations from a split of
 293 the solutions measured for their isotope composition are reported in Table 6. As the end-member
 294 phase compositions are known, mass balance constrains the fraction of magnetite contaminating the
 295 glass and is used to yield the isotope composition of the glass:

$$\delta^{51}V_{gl} = \frac{\delta^{51}V_{mix}(f_{mag}X_{mag}^V + (1-f_{mag})X_{gl}^V)}{f_{mag}\delta^{51}V_{mag}X_{mag}^V + (1-f_{mag})X_{gl}^V}. \quad (7)$$

297 Where X refers to the concentration of vanadium in magnetite and glass, and f their mass fraction.
 298 The mass fraction of magnetite is given by the two-phase mass balance:

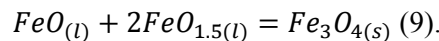
$$f_{mag} = \frac{(X_{mix}^V - f_{gl}X_{gl}^V)}{X_{mag}^V} \quad (8)$$

300 where X_{mix}^V is the concentration of V measured in solution. Values of X_{mix}^V , the total V_2O_3 in the
 301 mixture and those calculated for f_{mag} are listed in Table 6, with f_{mag} ranging from 5.3% in the HM
 302 experiment, and 0.4% in the NNO run, where the long run time permitted growth of magnetite and
 303 facilitated separation from the glass. The corrected $\delta^{51}V_{gl}$ values are in the range -1.02‰ (NNO) to -
 304 0.57‰ (HM) (Table 6). The true fractionation factor between magnetite and silicate glass
 305 ($\Delta^{51}V_{mag-gl}$) can then be calculated (Table 6).

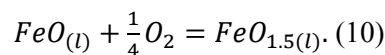
306 This quantity shows a negative dependence on the $\log fO_2$ of the experiment at 800°C, where
 307 $\Delta^{51}V_{mag-gl} = -0.92 \pm 0.11$ ‰ at $\log fO_2 = -9.68$ (HM) and where $\Delta^{51}V_{mag-gl} = -0.63 \pm 0.09$ ‰ at $\log fO_2$
 308 $= -15.74$ (FMQ-1), 1SD.

309 Partitioning and redox-dependence of Fe and V

310 Quantification of the co-ordination and oxidation state of V, in both magnetite and melt, is essential to
 311 understanding the direction and magnitude of isotopic fractionation between two phases. At
 312 equilibrium, the reaction describing the formation of magnetite from iron oxides present in a silicate
 313 melt is:



315 This demonstrates that the stoichiometry of Fe in magnetite is fixed and does not therefore depend on
 316 fO_2 . However, the relative proportions of the liquid components, $FeO_{(l)}$ and $FeO_{1.5(l)}$, depend on fO_2
 317 according to the reaction:



319 Assuming ideal (two-site) mixing for $Fe_3O_{4(s)}$, as is the case at high temperatures where Fe^{2+} and
 320 Fe^{3+} are randomly distributed over the A and B sites of magnetite (Wu and Mason, 1981), then
 321 $a(Fe_3O_4) = X(Fe_3O_4)^2$. Therefore, at equilibrium, equation (9) is written:

$$322 \quad 0 = 2\log X(Fe_3O_4) - 2\log X(FeO_{1.5}) - \log X(FeO) - \log K_{(1)}^*, \quad (11)$$

323 and for equation (10)

$$324 \quad 0 = \log X(FeO_{1.5}) - 0.25\log f(O_2) - \log X(FeO) - \log K_{(2)}^* \quad (12)$$

325 where $\log K^*$ denotes the deviation of the liquid components from ideality relative to the ideal case,
 326 $\log K$, in which $a = X$. Here, Henry's Law behaviour is assumed, such that $\frac{\gamma_{FeO_{1.5}}}{\gamma_{FeO}}$ is constant over all
 327 fO_2 , a condition shown to be valid for MORB (Berry et al., 2017).

328 With the constraint that $X(FeO_{1.5}) + X(FeO) = \sum FeO_x$, and given that $\sum FeO_x$, $X(Fe_3O_4)$ and fO_2
 329 are known from the experiments, a weighted non-linear least squares chi-squared minimisation is
 330 performed for the difference between the modelled and measured $\sum FeO_x$ by changing $\log K_{(9)}^*$ and
 331 $\log K_{(10)}^*$ and hence $X(FeO_{1.5})$ and $X(FeO)$:

$$332 \quad \chi^2 = \sum_i \left(\frac{\sum FeO_x^{calc} - \sum FeO_x^{obs}}{s(FeO_x)} \right)^2, \quad (13)$$

333 Where i denotes that the sum was performed globally for all four experiments simultaneously. The
 334 weighting of the uncertainty on the analyses, $s(FeO_x)$ was set to 0.15 of the $\sum FeO_x^{obs}$ value.

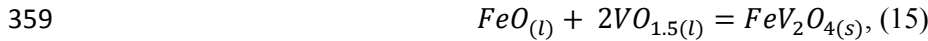
335 The calculated $\log K_{(9)}^* = 6.34 \pm 0.30$ and $\log K_{(10)}^* = 2.97 \pm 0.08$. The high $\log K_{(10)}^*$ relative to that
 336 determined for MORB at 1400°C and 1 bar (0.54; Berry et al., 2018), predominantly reflects the
 337 temperature-dependence of fO_2 . Corrected to a mineral buffer (FMQ; Fig. 3a), $Fe^{3+}/\sum Fe$ remains
 338 higher at a given fO_2 in hydrous haplogranite relative to MORB. In fact, the high $\log K_{(10)}^*$ is close to
 339 that found for the $K_2Si_3O_7$ and $Na_2Si_3O_7$ liquids studied at 1250°C and 1 bar by Knipping et al.
 340 (2015), suggesting that network-modifiers (Na, K) stabilise Fe^{3+} in silica-rich compositions (Thorner
 341 et al., 1980; Borisov et al., 2017).

342 Previous studies emphasise that trivalent V is significantly more compatible than V^{4+} or V^{5+} in silicate
 343 and oxide minerals (Canil, 1999; Nielsen et al., 1994; Righter et al., 2006b; Toplis and Corgne, 2002).
 344 This is due to the high octahedral site preference energy of V^{3+} ($4/5\Delta_{oct}$) and the suitability of its ionic
 345 radius in VI-fold co-ordination (0.645 Å) for $VI Fe^{3+}$ -occupied sites (0.64 Å). Magnetite, which has an
 346 inverse-spinel cation distribution at room temperature, $IV Fe^{2+} VI (Fe^{2+}, Fe^{3+}) O_4$ (e.g., Bosi et al., 2009;
 347 Fleet, 1981), tends towards a random (normal) structure at high temperatures (Wu and Mason, 1981),
 348 and V is incorporated as the coulsonite end-member, which is a normal spinel; $IV Fe^{2+} VI (V^{3+})_2 O_4$

349 (Radtke, 1962). With both the ferric-ferrous and $V^{3+/4+}$ redox pairs present, the following reaction
 350 occurs in magnetite:



352 At high temperatures, the equilibrium constant tends to 1 (a statistically random arrangement) because
 353 having substantial fractions of each of the four species results in particularly high configurational
 354 entropy. As the free energy associated with electron exchange is small, this causes a large, negative
 355 deviation from ideality of mixing, meaning the substitution of V^{3+} in magnetite is energetically more
 356 favourable than either of the end-members (Fe_3O_4 or FeV_2O_4). As temperature decreases, the reactants
 357 become progressively favoured (Wakihara and Katsura, 1971; O'Neill and Navrotsky, 1984), and the
 358 substitution of V into magnetite can be written:



360 demonstrating that the incorporation of V is also independent of fO_2 . At equilibrium, in the system Fe-
 361 V-O, eq. 15 becomes:

$$362 \quad 0 = 2\log(1 - XFe_3O_4) - 2\log X(VO_{1.5}) - \log X(FeO) - \log K_{(7)}^*. \quad (16)$$

363 The mole fraction of $VO_{1.5}$ in the silicate melt, and resultant V^{3+}/V^{4+} ratio, is in turn dependent on the
 364 fO_2 of the experiment:



367 and, at equilibrium:

$$368 \quad 0 = \log X(VO_2) - 0.25 \log f(O_2) - \log X(VO_{1.5}) - \log K_{(17)}^*. \quad (19)$$

$$369 \quad 0 = \log X(VO_{2.5}) - 0.25 \log f(O_2) - \log X(VO_2) - \log K_{(18)}^*. \quad (20)$$

370 As V is a trace element in the silicate melt, it is assumed to be in the Henry's Law region, where the
 371 activity coefficient for each valence is independent of fO_2 . The constraint that $X(VO_{1.5}) + X(VO_2) +$
 372 $X(VO_{2.5}) = \sum VO_x$ enables a global non-linear least-squares fit to be performed to the $\sum VO_x$
 373 measured in the silicate melt, analogous to that described for iron (eq. 13). Calculated equilibrium
 374 constants are $\log K_{(15)}^* = 11.09 \pm 0.19$; $\log K_{(17)}^* = 5.04 \pm 0.12$ and $\log K_{(18)}^* = 2.65 \pm 0.10$. The high
 375 equilibrium constant of eq. 15 reflects the stability of the FeV_2O_4 component in magnetite. The
 376 $\log K_{(17)}^* - \log K_{(18)}^* = 2.39$ shows that V^{4+} is the dominant oxidation state of V in silicate liquids (e.g.
 377 Giuli *et al.*, 2004; Sutton *et al.*, 2005), except under highly oxidising conditions ($>FMQ+3$; Table 7,
 378 Fig. 3b).

379 Values of $\log K^*$ in this work are generally lower (i.e., favouring the reduced species) than found in
 380 Toplis and Corgne (2002) for a ferrobasaltic composition at 1068°C and 1 bar, see Table 7. This
 381 behaviour is a reflection of the lower slope in a $\log(D_V)$ vs. ΔFMQ diagram (Fig. 4), where m , the
 382 slope, is dictated by the change of speciation of V in the liquid (a slope of -0.31 denotes $\sum D_V = D_{V^{3+}}$,
 383 with lower slopes reflecting increasing $D_{V^{4+}}$). For the data of Toplis and Corgne (2002) $m = -0.30$
 384 compared with -0.16 herein. However, we note that the omission of their most oxidised experiment
 385 would decrease their slope to -0.18, in much closer agreement with our data. This reduction in slope
 386 equates to $D_{V^{3+}} = 3070$ and $D_{V^{4+}} = 64$, hence $D_{V^{4+}}/D_{V^{3+}} = 2.1\%$, somewhat higher than the 0.2-0.5%
 387 (or 1% for a slope of -0.18) obtained by Toplis and Corgne (2002). By contrast, the slope of the data
 388 defined by the data of Sievwright *et al.*, (2017) for andesitic-dacitic melts at 1070°C, 1 bar and Arató
 389 and Audétat (2017) are steeper again, near -0.50; higher than the maximum of -0.30 allowed.
 390 Nevertheless, especially at high fO_2 , our values of D_V compare well with Arató and Audétat (2017),
 391 whose experiments were run under essentially the same conditions (800°C, 5 kb) and compositions
 392 (haplogranite with ASI of ≈ 1). A slope of -0.50 implies that vanadium is exclusively V^{3+} in magnetite
 393 and V^{5+} in the melt. This differing behaviour may arise due to the high FeV_2O_4 component in our
 394 experiments and those of Toplis and Corgne (2002), compared with the trace amount of V present in
 395 magnetite in Sievwright *et al.*, (2017) and Arató and Audétat (2017), where increasing V^{3+} pushes
 396 equilibrium (14) to the left, producing V^{4+} . In natural titanomagnetites crystallising from layered
 397 mafic intrusions (*e.g.*, Balan *et al.*, 2006) $V^{3+}/\sum V$ ranges from 0.83 to 0.98, consistent with the
 398 preference of V^{3+} for magnetite. Together, these results confirm that $D_{V^{3+}} \gg D_{V^{4+}}$ as expected
 399 thermodynamically.

400 Controls on V isotope fractionation

401 Isotopic fractionation can be understood in the context of the bond valence model, which states that
 402 the sum of the bond valence ($s = \text{charge/co-ordination}$) must equal the formal charge on the ion
 403 (Pauling, 1929). Its relation to the strength of the $\langle V-O \rangle$ bonds (the parameter that controls isotope
 404 fractionation) is given by the force constant, K_f , which may be approximated by describing the
 405 bonding environment of V by electrostatic interactions, using the Born-Landé equation (see Young *et al.*
 406 *et al.*, 2009; Sossi and O'Neill, 2017):

$$407 \quad K_{f,v,o} = -\frac{\bar{s}_V \bar{s}_O q^2 (1-n)}{4\pi \epsilon_o r^3} \quad (21)$$

408 Here, ϵ_o is the permittivity of free space, q the charge on an electron in coulombs, B the Born
 409 exponent (=12 in minerals, Young *et al.*, 2009) and r the radius in metres. The force constant
 410 therefore increases (which favours heavier isotopes) as charge increases or co-ordination decreases
 411 because both phenomena are associated with a shortening of the bond length.

412 Calculations performed herein are benchmarked against recent molecular dynamics simulations of
 413 hydrated V species of variable oxidation state (Wu et al., 2015) and compare favourably (see
 414 Appendix A for details). At high temperatures, the force constant can be related to the reduced
 415 partition function ratio, or β factor, by a constant term, f that describes the quantum component of the
 416 partition function ratio, and is dependent on the relative mass difference between the two isotopes
 417 (Bigeleisen and Mayer, 1947):

$$f = \frac{3N_A 10^3}{96\pi^2} \left(\frac{h}{k_B T} \right)^2 \left(\frac{1}{m_n} - \frac{1}{m_d} \right), \quad (22)$$

419 where N_A is Avogadro's number, h is Planck's constant, k_B Boltzmann's constant, m the molar mass,
 420 and for $^{51}\text{V}/^{50}\text{V} = 1720$; and the temperature, in Kelvin, squared:

$$10^3 \ln \beta_V^{51/50} = \frac{1720(K_f)}{T^2}. \quad (23)$$

422 While the oxidation state of V in magnetite and co-existing melt can be estimated (see *Partitioning*
 423 *and redox-dependence of Fe and V*), information on co-ordination number and bond lengths is rare
 424 (Schindler et al., 2000). As in minerals, V^{3+} is octahedrally co-ordinated in basaltic glasses, V^{4+} has an
 425 average co-ordination of 5.33 (Sutton et al., 2005), whereas V^{5+} -O bond lengths are 1.82Å (close to
 426 V-fold), decreasing to 1.7±0.02Å (IV-fold) in alkali- and Ca-rich compositions (Giuli et al., 2004).
 427 This figure closely matches that obtained by adding the ionic radii of $^{IV}\text{V}^{5+}$ (0.355Å) and O^{2-} (1.38Å),
 428 1.74Å. In the experimental glasses r is therefore estimated by linear interpolation between $\langle\text{V-O}\rangle$
 429 bond distances for V^{5+} ($r = 1.74$ Å) and V^{4+} ($r = 1.87$ Å) (Giuli et al., 2004; Sutton et al., 2005), with
 430 values shown in Table 8.

431 The constancy of V oxidation state, and hence calculated $\langle\text{V-O}\rangle$ bond lengths in magnetite over the
 432 range of $f\text{O}_2$ investigated means that changes in V speciation in the melt control the degree of isotopic
 433 fractionation. Results of these calculations (Fig. 5) show that an average oxygen co-ordination of 2.5
 434 best fits the melt experimental data, implying a network-forming role for both V^{4+} and V^{5+} , which is
 435 unsurprising given their similar charge and co-ordination to Si^{4+} . Importantly, the model also predicts
 436 that magnetite, where V exists in a lower average valence (3+) and higher co-ordination (VI-fold),
 437 should always be isotopically *lighter* than co-existing melt. The model reproduces the larger isotopic
 438 fractionation observed in the more oxidised experiments, where the difference in charge, co-
 439 ordination and $\langle\text{V-O}\rangle$ bond length is greater between the two phases at higher $f\text{O}_2$.

440 Figure 5 illustrates the dependence of the fractionation factor between magnetite and melt as a
 441 function of $f\text{O}_2$ at 800°C, which has the form:

$$\Delta^{51}\text{V}_{\text{Mag-Melt}} (\text{‰}) = -0.045 \pm 0.021(\Delta FMQ) - 0.70 \pm 0.05 \quad (24)$$

443 Uncertainties take into account the errors on the analyses themselves as well as the goodness of fit of
1 444 the regression, and should be noted that they are compensatory (a positive uncertainty in the slope is
2 445 compensated for by a negative uncertainty in the intercept, and vice-versa). The slope illustrates that
3 446 the dependence on fO_2 is small over the range of igneous rocks as V remains V^{3+} in magnetite but
4 447 increases in valence in the melt. Fractionation is largely driven by i) the difference in redox state of
5 448 trivalent V in magnetite and V^{4+}/V^{5+} in the melt over a range of fO_2 , and ii) the difference in co-
6 449 ordination between octahedral V^{3+} in magnetite and IV- to V-fold co-ordinated V in the liquid.

450 **Implications**

451 **Comparison with natural data**

452 Minerals in the titanomagnetite solid solution are common accessory phases in igneous systems on
18 453 Earth. Despite their minor abundance, the timing of their appearance on the liquid line of descent
19 454 gives rise to the distinct chemical evolution of the tholeiitic (late saturation, iron-enrichment) and
20 455 calc-alkaline (early saturation, iron depletion) magmatic trends (Sisson and Grove, 1993). As the
21 456 timing of this saturation is dependent on the fO_2 of the crystallising magma (e.g., Toplis and Carroll,
22 457 1995; Feig et al., 2010), magnetite may provide an important record of the prevailing oxygen fugacity
23 458 via its vanadium isotope composition. Furthermore, magnetite crystallisation reduces the melt by
24 459 preferentially sequestering Fe^{3+} and can trigger sulphide saturation with important implications for the
25 460 formation of economically viable mineral deposits (e.g., Jenner et al., 2010).

33 461 Prytulak et al. (2017) measured the whole rock V isotope composition of two differentiating
34 462 magmatic suites from Hekla, Iceland and Anatahan volcano, from the Marianas island arc. The former
35 463 records $fO_2 \approx FMQ$ (Baldrige, 1974) whereas magmas from the Marianas crystallise under a more
36 464 oxidised regime, near FMQ+2 (Brounce et al., 2014). Despite these differing oxygen fugacities, the V
37 465 isotope evolution in both systems shows a similar trajectory, in which the most differentiated magmas
38 466 reach $\delta^{51}V_{AA} \sim +1\%$ from an initial, parent magma composition of near -0.7% . In detail, the
39 467 calculated magnetite-melt fractionation factors differ slightly; -0.5% for Anatahan, and -0.45% for
40 468 Hekla (Prytulak et al., 2017) at $\approx 1000^\circ C$.

47 469 Strikingly, however, both of these fractionation factors derived from bulk lavas fall in the range
48 470 determined experimentally herein. Using the correlation of the experimental fractionation factor with
49 471 fO_2 (eq. 24), corrected from $800^\circ C$ to $1000^\circ C$ assuming a $1/T^2$ dependence (eq. 23), gives relative fO_2
50 472 of FMQ-1.5 for Hekla and FMQ+0.7 for Anatahan, in excellent agreement with the 2 log unit
51 473 difference recorded by oxygen barometry (see Prytulak et al., 2017, and references therein), although
52 474 they are displaced to lower values (FMQ and FMQ+2, respectively). It remains to be explored as to
53 475 whether changes in composition in the melt phase affect V redox and co-ordination, and hence the
54 476 isotopic fractionation factor. That melt composition can alter co-ordination number was shown for Fe,

477 where IV-fold co-ordinated iron is preferred relative to VI-fold in more polymerised, alkali-rich
478 rhyolitic compositions with respect to more mafic compositions (Dauphas et al. 2014). A similar
479 effect may be expected for V, because the low bond valence alkalis stabilise lower V co-ordination
480 numbers (see Jackson et al., 2005). Indeed, Giuli et al. (2004) observed that in Fe-bearing
481 compositions, V^{5+} was in higher co-ordination than in Fe-free and sodium-silicate compositions. The
482 stronger $\langle V-O \rangle$ bonds found in lower co-ordination environments would therefore produce greater
483 $\Delta^{51}V_{\text{mag-melt}}$ fractionation in granitic melts compared with basaltic liquids. Empirically, given the
484 displacement in calculated fO_2 with respect to measured values in Hekla and Anatahan suggests that
485 the fractionation factor may indeed be sensitive to composition. If so, then the experimental
486 calibration for haplogranitic compositions is not directly applicable to the andesitic-dacitic liquids
487 crystallising at Hekla and Anatahan. Nevertheless, the fO_2 dependence (the slope in eq. 24) will be
488 less sensitive to composition because different melt components will affect the $\log K^*$ of eqs. 15, 17
489 and 18 by altering the vanadium oxide activity coefficients in the melt ($\gamma VO_{1.5}$, γVO_2 and $\gamma VO_{2.5}$) but
490 not the stoichiometries of the reactions.

491 The relative insensitivity of the V isotope composition in whole rock lavas to their different redox
492 states shows that V isotopes are not straightforward indicators of fO_2 variations in igneous systems.
493 However, the systematic increase in fractionation factor with fO_2 (Fig. 2), is potentially resolvable if
494 magnetite-melt pairs are determined. In the absence of the melt phase, because magnetite commonly
495 hosts the majority of the vanadium in crystallising magmas, it may act as a single mineral indicator of
496 fO_2 .

497 **Magnetite as an indicator of fO_2**

498 Given the diverse ways in which magnetite may form on the Earth, the chemistry of this mineral
499 likely holds clues to its provenance and conditions of formation. However, discrimination of
500 magnetite provenance based trace elements alone can be troublesome given that igneous magnetite
501 may span a wide range of composition dependent on its petrogenetic history, resulting in the overlap
502 of many trace element fingerprints in different formation environments (e.g., Dare et al., 2012).

503 Magnetite from igneous rocks are amongst the most V-rich on Earth, often containing > 0.15 wt. %
504 V_2O_3 , and reaching levels of several weight percent in some settings such as layered mafic intrusions
505 (e.g. Grigsby, 1990; Dare et al., 2014; Toplis and Corgne, 2002; Balan et al., 2006). Figure 6 depicts
506 results of a fractional crystallisation model similar to Prytulak et al. (2017) to predict the V isotope
507 composition of magnetite at different fO_2 conditions. The fO_2 of an initial ferrobaltic magma with
508 6.5 wt. % MgO, 12 wt. % FeO and 300 ppm V (Toplis and Corgne, 2002), is varied from FMQ-1,
509 FMQ+1 to FMQ+3 (Fig. 6). Temperature is related to the fraction of melt, F , by the expression $T^\circ C =$
510 $1022+266(F)-290F^2+175F^3$ (Toplis and Corgne, 2002). Magnetite saturation (at $T^\circ C <$

511 27.2×ΔNNO+1125) and modal abundance (ol+plag):cpx:mag =42:40:18, as a function of fO_2 and
512 temperature, is parameterised after Toplis and Corgne (2002), while olivine and augite Mg#s are
513 given by $K_D^{Fe-Mg} = 0.3$ (Toplis, 2005; Bédard, 2010). Plagioclase is the only other mineral to
514 crystallise, with phase proportions set to ol:plag = 0.27 and ol:(cpx+plag) = 0.27 (Toplis and Carroll,
515 1995). Partition coefficients as a function of fO_2 for V in magnetite are taken from this work and those
516 for clinopyroxene from Mallmann and O'Neill (2009). The vanadium isotope fractionation factor
517 between magnetite and melt is taken from equation (24), and is assumed to apply to clinopyroxene-
518 melt due to its preference for trivalent V in octahedral co-ordination (Karner et al., 2005; Mallmann
519 and O'Neill, 2009). At FMQ-1, clinopyroxene crystallises first, depriving the melt of half its V budget
520 before magnetite crystallises ($D_V = 63.1$) with a maximum of 1.4 wt. % V_2O_3 . Intermediate fO_2
521 produces the greatest enrichment of V in magnetite (1.51 wt. %) despite lower D_V , of 26.9, as it co-
522 crystallises with augite. At FMQ+3, magnetite is initially poor in V_2O_3 (0.57 wt. %) owing to its
523 lower D_V of 12.6, but the melt is depleted more slowly, such that magnetite crystallising at the end of
524 differentiation is still V-rich (>100 ppm). Magnetite from the reduced series has the heaviest $\delta^{51}V$,
525 owing to a) extraction of light V into clinopyroxene and b) rapid depletion of V from the melt (Fig. 6).
526 In general, magmatic magnetite will be initially light and V-rich, before evolving to heavy, V-poor
527 compositions due to progressive extraction of V by magnetite (\pm clinopyroxene).

528 Granitic rocks, whose compositions range from reduced, A-type granites (Turner et al., 1992; Frost
529 and Frost, 2010) to oxidised, magnetite-bearing I-type granite (Chappell and White, 1977) may evolve
530 distinct V isotope signatures in magnetite. Qualitatively, the protracted fractionation crystallisation
531 that produces A-types (*e.g.*, Turner et al., 1992; Shellnutt et al., 2009) depletes the remaining melt in
532 V and light V isotopes, such that any magnetite to crystallise from these evolved magmas is V-poor
533 (<100 ppm) and inherits a heavy isotope composition, >1.5‰ (Fig. 6). By contrast, magnetite in I-
534 type granites, owing to their more oxidising environment, crystallises earlier in its magmatic evolution
535 while ample V remains in the melt. This melt is still isotopically light, akin to basaltic liquids
536 (Prytulak et al., 2013; Fig. 6), and the $\Delta^{51}V_{mag-melt}$ fractionation factor upon magnetite precipitation is
537 enhanced due to the oxidising conditions, resulting in isotopically light magnetite, $\leq 1\%$ (Fig. 6) that
538 is relatively rich in V (>100 ppm). This behaviour mirrors that observed for iron isotopes in granitic
539 rocks (Foden et al., 2015). The isotopic composition of V in detrital, igneous magnetite may therefore
540 prove diagnostic in identifying the conditions under which it crystallised from its parent magma,
541 which may be especially useful in older Archean rocks in which magnetite is often detrital.

542 Magnetite precipitated from high temperature (500 – 800 °C) porphyry fluids may reach similar V_2O_3
543 contents (≈ 0.5 wt. %; *e.g.* Nadoll et al., 2014) to those found in mafic igneous rocks. Vanadium
544 contents decrease to ≈ 0.1 wt. % (Canil et al., 2016) in magnetite associated with skarn-type
545 mineralisation (300 – 500°C). The lowest V contents (and trace elements in general) occur in

546 magnetite precipitated from seawater to comprise BIFs (Dare et al., 2014; Nadoll et al., 2014), with a
547 median of 4.8 ppm (-4.5/+36, $n = 135$). The diversity of magnetite V concentrations forming in
548 distinct environments at different temperatures offers ample scope for stable isotopic fractionation.
549 Therefore, characterisation of the V isotope composition of magnetite formed in different settings
550 may in the future, together with V concentrations, act as a powerful provenance tracer.

551 **Conclusion**

552 The first V isotope fractionation factors between experimentally-grown magnetite and hydrous,
553 haplogranitic melts at 800°C, 0.5 GPa were determined. Oxygen fugacity in the experiments was
554 varied by fixing fH_2 according to different mineral buffers, varying from FMQ-1 to FMQ+5,
555 supplemented by a 1 atm run with an alkali-silica melt at FMQ-1. Vanadium becomes more
556 compatible in magnetite at progressively more reducing conditions in response to a higher abundance
557 of V^{3+} in the granitic melt. This behaviour is reflected in increasingly isotopically heavy melt relative
558 to magnetite at higher fO_2 , ranging from $\Delta^{51}V_{\text{mag-gl}} = -0.63 \pm 0.09\text{‰}$ at FMQ-1 to $-0.92 \pm 0.11\text{‰}$ at
559 \approx FMQ+5, and can be fit by $\Delta^{51}V (\text{‰}) = -0.045 \pm 0.021 \times \Delta\text{FMQ} - 0.70 \pm 0.05$. Such a trend can be
560 reproduced by modelling the fractionation factor according to the bond valence model, where V is
561 $^{VI}V^{3+}$ in magnetite, and a mixture of IV- and VI-fold V^{5+} and V^{4+} in the melt. Experimentally-derived
562 fractionation factors are in accord with those inferred from natural systems, highlighting the role of
563 magnetite in controlling the V isotope composition of evolving magmatic systems. The ubiquity of
564 magnetite on the Earth's surface and its formation in igneous, metamorphic, hydrothermal, and
565 aqueous environments likely engenders significant isotopic fractionation.

566 **Acknowledgements**

567 PAS was funded by an Australian Postgraduate Award and an ANU Vice-Chancellor's Scholarship.
568 Analytical costs and JPs visit to ANU were funded by Australian Research Council Discovery Grant
569 DP130101355 to H. St.C. O'Neill and J. Prytulak. Many thanks to Jeremy Wykes, Dave Clark and
570 Dean Scott for discussions regarding the piston cylinder experiments, Graham Mortimer for
571 facilitating the set-up of V isotopes at the RSES clean lab, and Les Kinsley for assistance and
572 feedback on running V isotopes on the Neptune Plus. We greatly appreciate two thoughtful and
573 comprehensive reviews by Alan Woodland and Dante Canil that helped improve many aspects of this
574 study, and acknowledge perceptive comments from Adrian Fiege on an earlier version of this work.
575 We are grateful to Othmar Müntener for his exemplary editorial handling.

576 **References**

577 Anbar AD, Roe JE, Barling J, Nealson KH (2000) Nonbiological Fractionation of Iron Isotopes. *Science*, 288:126–128.

- 578 Arató R, Audétat A (2017) Experimental calibration of a new oxybarometer for silicic magmas based on vanadium
579 partitioning between magnetite and silicate melt. *Geochim Cosmochim Acta*, 209:284-295.
- 580 Ardia P, Giordano D, Schmidt MW (2008) A model for the viscosity of rhyolite as a function of H₂O-content and pressure:
581 A calibration based on centrifuge piston cylinder experiments. *Geochim Cosmochim Acta*, 72:6103-6123.
- 582 Balan E, De Villiers JPR, Eeckhout SG, Glatzel P, Toplis MJ, Fritsch E, Allard T, Galois L, Calas G (2006) The oxidation
583 state of vanadium in titanomagnetite from layered basic intrusions. *Am Mineral* 91:953-956.
- 584 Baldrige WS, McGetchin TR, Frey FA, Jarosewich E (1973) Magmatic evolution of Hekla, Iceland. *Contrib Mineral
585 Petrol*, 42(3):245-258.
- 586 Bédard JH (2010) Parameterization of the Fe-Mg exchange coefficient (K_D) between clinopyroxene and silicate melts. *Chem
587 Geol*, 274(3-4):169-176.
- 588 Behrens H, Jantos N (2001) The effect of anhydrous composition on water solubility in granitic melts. *Am Mineral* 86(1-
589 2):14-20.
- 590 Berry AJ, Stewart GA, O'Neill HSC, Mallmann G, Mosselmans JFW (2018) A re-assessment of the oxidation state of iron
591 in MORB glasses. *Earth Planet Sci Lett* 483:114-123.
- 592 Bigeleisen J, Mayer MG (1947) Calculation of equilibrium constants for isotopic exchange reactions. *J Chem Phys*,
593 15(5):261-267.
- 594 Boettcher AL, Mysen BO, Allen JC (1973) Techniques for the control of water fugacity and oxygen fugacity for
595 experimentation in solid-media high-pressure apparatus. *J Geophys Res* 78:5898-5901.
- 596 Borisov A, Behrens H, Holtz F (2017) Effects of strong network modifiers on Fe³⁺/Fe²⁺ in silicate melts: an experimental
597 study. *Contrib Mineral Petrol* 172(5):34.
- 598 Bosi F, Halenius U, Skogby H (2009) Crystal chemistry of the magnetite-ulvospinel series. *Am. Mineral.* 94:181-189.
- 599 Boutroy E, Dare SAS, Beaudoin G, Barnes S-J, Lightfoot PC (2014) Magnetite composition in Ni-Cu-PGE deposits
600 worldwide: application to mineral exploration. *J Geochem Exp* 145:64-81.
- 601 Bowen NL, Schairer JF, Willems HMV (1930) The Ternary System Na₂SiO₃-Fe₂O₃-SiO₂. *Am J Sci* 20:405-455.
- 602 Brounce MN, Kelley KA, Cottrell E (2014) Variations in Fe³⁺/ΣFe of Mariana Arc Basalts and Mantle Wedge fO₂. *J Petrol*,
603 55(12):2513-2536.
- 604 Canil D (1997) Vanadium partitioning and the oxidation state of Archean komatiite magmas. *Nature*, 389:842-845.
- 605 Canil D (1999) Vanadium partitioning between orthopyroxene, spinel and silicate melt and the redox states of mantle source
606 regions for primary magmas. *Geochim Cosmochim Acta* 63:557-572.
- 607 Canil D (2004) Mildly incompatible elements in peridotites and the origins of mantle lithosphere. *Lithos* 77:375-393.
- 608 Canil D, Grondahl C, Lacourse T, Pisiak LK (2016) Trace elements in magnetite from porphyry Cu-Mo-Au deposits in
609 British Columbia, Canada. *Ore Geol Rev* 72:1116-1128.
- 610 Carmichael ISE (1991) The redox states of basic and silicic magmas: a reflection of their source regions? *Contrib to Mineral
611 Petrol* 106:129-141.
- 612 Chappell BW, White AJR (1974) Two contrasting granite types. *Pacific Geology* 8:173-174
- 613 Chou I-M (1986) Permeability of precious metals to hydrogen at 2 kb total pressure and elevated temperatures. *Am J Sci*
614 286:638-658.
- 615 Dare SAS, Barnes S-J, Beaudoin G (2012) Variation in trace element content of magnetite crystallized from a fractionating
616 sulfide liquid, Sudbury, Canada: Implications for provenance discrimination. *Geochim Cosmochim Acta*, 88:27-50.

- 1 617 Dare SAS, Barnes S-J, Beaudoin G, Meric J, Boutroy E, Potvin-Doucet C (2014) Trace elements in magnetite as
2 618 petrogenetic indicators. *Miner Deposita*, 49:785-796.
- 3 619 Dauphas N, Roskosz M, Alp EE, Neuville DR, Hu MY, Sio CK, Zhao J, Tissandier L, Médard E, Cordier C (2014). Magma
4 620 redox and structural controls on iron isotope variations in Earth's mantle and crust. *Earth Planet Sci Lett*, 398:127-140.
- 5
6 621 Eugster HP (1957) Heterogeneous Reactions Involving Oxidation and Reduction at High Pressures and Temperatures. *J*
7 622 *Chem Phys* 26:1760–1761.
- 8
9 623 Feig ST, Koepke J, Snow JE (2010) Effect of oxygen fugacity and water on phase equilibria of a hydrous tholeiitic basalt.
10 624 *Contrib Mineral Petrol* 160(4):551-568.
- 11
12 625 Fleet ME (1981) The Structure of Magnetite. *Acta Crystallogr B*37:917–920.
- 13
14 626 Frost CD, Frost BR (2010) On ferroan (A-type) granitoids: their compositional variability and modes of origin. *J Petrol*,
15 627 52(1):39-53.
- 16
17 628 Fuchs JN (1825) Ueber ein neues Product aus Kieselerde und Kali. *Arch Für die gesammte Naturlehre* 5:385–412.
- 18
19 629 Giuli G, Paris E, Mungall JE, Romano C, Dingwell DB (2004) V oxidation state and coordination number in silicate glasses
20 630 by XAS. *Am Mineral* 89:1640–1646.
- 21
22 631 Grigsby JD (1990) Detrital magnetite as a provenance indicator. *J Sediment Res* 60:940-951
- 23
24 632 Holtz F, Johannes W, Tamic N, Behrens H (2001) Maximum and minimum water contents of granitic melts generated in the
25 633 crust: a reevaluation and implications. *Lithos* 56:1–14.
- 26
27 634 Jackson WE, Farges F, Yeager M, Mabrouk PA, Rossano S, Waychunas GA, Solomon EI, Brown Jr GE (2005) Multi-
28 635 spectroscopic study of Fe (II) in silicate glasses: Implications for the coordination environment of Fe (II) in silicate
29 636 melts. *Geochim Cosmochim Acta*, 69(17):4315-4332.
- 30
31 637 Jarosewich E, Nelen JA, Norberg JA (1980). Reference Samples for Electron Microprobe Analysis. *Geostand Geoanalytical*
32 638 *Res* 4:43–47.
- 33
34 639 Jenner FE, O'Neill HSC, Arculus RJ, Mavrogenes JA (2010) The magnetite crisis in the evolution of arc-related magmas
35 640 and the initial concentration of Au, Ag and Cu. *J Petrol*, 51(12):2445-2464.
- 36
37 641 Karner J, Papike JJ, Shearer CK (2006) Comparative planetary mineralogy: Pyroxene major-and minor-element chemistry
38 642 and partitioning of vanadium between pyroxene and melt in planetary basalts. *Am Mineral*, 91(10):1574-1582.
- 39
40 643 Knipping JL, Behrens H, Wilke M, Goettlicher J, Stabile P (2015) Effect of oxygen fugacity on the coordination and
41 644 oxidation state of iron in alkali bearing silicate melts. *Chem Geol* 411:143-154.
- 42
43 645 Lee C-TA, Leeman WP, Canil D, Li ZXA (2005) Similar V/Sc Systematics in MORB and Arc Basalts: Implications for the
44 646 Oxygen Fugacities of their Mantle Source Regions. *J Petrol* 46:2313–2336.
- 45
46 647 Mallmann G, O'Neill HSC (2009) The Crystal/Melt Partitioning of V during Mantle Melting as a Function of Oxygen
47 648 Fugacity Compared with some other Elements (Al, P, Ca, Sc, Ti, Cr, Fe, Ga, Y, Zr and Nb). *J Petrol* 50:1765–1794.
- 49
50 649 Mallmann G, O'Neill HSC (2013) Calibration of an Empirical Thermometer and Oxybarometer based on the Partitioning of
51 650 Sc, Y and V between Olivine and Silicate Melt. *J Petrol*, 54(5):933-949.
- 52
53 651 Massalski TB (1990) Binary Alloy Phase Diagrams, 2nd ed. ASM International, Materials Park, Ohio.
- 54
55 652 Matjuschkin V, Brooker RA, Tattitch B, Blundy JD, Stamper CC (2015) Control and monitoring of oxygen fugacity in
56 653 piston cylinder experiments. *Contrib to Mineral Petrol*, 169:1-16.
- 57
58 654 Medard E, McCammon CA, Barr JA, Grove TL (2008) Oxygen fugacity, temperature reproducibility, and H₂O contents of
59 655 nominally anhydrous piston-cylinder experiments using graphite capsules. *Am Mineral* 93:1838–1844.
- 60
61
62
63
64
65

- 1 656 Muan A (1963) Silver-Palladium Alloys As Crucible Material in Studies of Low-Melting Iron Silicates. *Ceram Bull* 42:344–
2 657 347.
- 3 658 Mungall JE (2002) Empirical models relating viscosity and tracer diffusion in magmatic silicate melts. *Geochim Cosmochim*
4 659 *Acta*, 66(1):125-143.
- 5
6 660 Nadoll P, Angerer T, Mauk JL, French D, Walshe J (2014) The chemistry of hydrothermal magnetite: a review. *Ore Geol*
7 661 *Rev* 16:1-32.
- 8
9 662 Nielsen RL, Forsythe LM, Gallahan WE, Fisk MR (1994) Major- and trace-element magnetite-melt equilibria. *Chem Geol*
10 663 117:167–191.
- 11
12 664 Nielsen SG, Prytulak J, Halliday AN (2011) Determination of Precise and Accurate $^{51}\text{V}/^{50}\text{V}$ Isotope Ratios by MC-ICP-MS,
13 665 Part 1: Chemical Separation of Vanadium and Mass Spectrometric Protocols. *Geostand Geoanalytical Res* 35:293–
14 666 306.
- 15
16 667 Nielsen SG, Prytulak J, Wood BJ, Halliday AN (2014) Vanadium isotopic difference between the silicate Earth and
17 668 meteorites. *Earth Planet Sci Lett* 389:167-175.
- 18
19 669 Nielsen SG, Owens JD, Horner TJ (2016) Analysis of high-precision vanadium isotope ratios by medium resolution MC-
20 670 ICP-MS. *J Anal At Spectrom*, 31:531-536
- 21
22 671 O'Neill HSC, Navrotsky A (1984) Cation distributions and thermodynamic properties of binary spinel solid solutions. *Am*
23 672 *Mineral* 69:733–753.
- 24
25 673 O'Neill HSC (1987) Quartz-fayalite-iron and quartz-fayalite-magnetite equilibria and the free energy of formation of fayalite
26 674 (Fe_2SiO_4) and magnetite (Fe_3O_4). *Am Mineral* 72(1-2):67-75.
- 27
28 675 Parkinson IJ, Arculus RJ (1999) The redox state of subduction zones: insights from arc-peridotites. *Chem Geol* 160:409–
29 676 423.
- 30
31 677 Pauling L, (1929) The Principles Determining the Structure of Complex Ionic Crystals. *J Am Chem Soc* 51:1010–1026.
- 32
33 678 Petric A, Jacob KT (1982). Thermodynamic Properties of Fe_3O_4 - FeV_2O_4 and Fe_3O_4 - FeCr_2O_4 Spinel Solid Solutions. *J Am*
34 679 *Ceram Soc* 65(2):117-123.
- 35
36 680 Prytulak J, Nielsen SG, Halliday AN (2011) Determination of Precise and Accurate $^{51}\text{V}/^{50}\text{V}$ Isotope Ratios by Multi-
37 681 Collector ICP-MS, Part 2: Isotopic Composition of Six Reference Materials plus the Allende Chondrite and
38 682 Verification Tests. *Geostand Geoanalytical Res* 35:307–318.
- 39
40 683 Prytulak J, Nielsen SG, Ionov DA, Halliday AN, Harvey J, Kelley KA, Niu Y, Peate DW, Shimizu K, Sims KWW (2013)
41 684 The stable vanadium isotope composition of the mantle and mafic lavas. *Earth Planet Sci Lett* 365:177–189.
- 42
43 685 Prytulak J, Sossi PA, Halliday AN, Plank T, Savage PS, Woodhead JD (2017) Stable vanadium isotopes as a redox proxy in
44 686 magmatic systems? *Geochem Persp Lett*, 3(1):75-84.
- 45
46 687 Radtke AS (1962) Coulsonite, FeV_2O_4 , A Spinel-Type Mineral from Lovelock, Nevada. *Am Mineral* 47:1284–1291.
- 48
49 688 Righter K, Sutton SR, Newville M, Le L, Schwandt C, Uchida H, Lavina B, Downs RT (2006a) An experimental study of
50 689 the oxidation state of vanadium in spinel and basaltic melt with implications for the origin of planetary basalt. *Am*
51 690 *Mineral* 91, 1643–1656.
- 52
53 691 Righter K, Leeman W, Hervig R (2006b) Partitioning of Ni, Co and V between spinel-structured oxides and silicate melts:
54 692 Importance of spinel composition. *Chem Geol* 227:1–25.
- 55
56 693 Schauble E (2004) Applying stable isotope fractionation theory to new systems. *Rev Mineral Geochem* 55:65-111.
- 57
58 694 Schindler M, Hawthorne FC, Baur WH (2000) Crystal Chemical Aspects of Vanadium: Polyhedral Geometries,
59 695 Characteristic Bond Valences, and Polymerization of (Von) Polyhedra. *Chem Mater* 12:1248–1259.
- 60
61
62
63
64
65

- 696 Schuth S, Horn I, Brüske A, Wolff PE, Weyer S (2017). First vanadium isotope analyses of V-rich minerals by femtosecond
697 laser ablation and solution-nebulization MC-ICP-MS. *Ore Geo Rev*, 81:1271-1286.
- 698 Shannon RT (1976) Revised effective ionic radii and systematic studies of interatomic distances in halides and
699 chalcogenides. *Acta Crystall A*, 32(5):751-767.
- 700 Shellnutt JG, Zhou MF, Zellmer GF (2009) The role of Fe–Ti oxide crystallization in the formation of A-type granitoids
701 with implications for the Daly gap: an example from the Permian Baima igneous complex, SW China. *Chem Geol*,
702 259(3-4):204-217.
- 703 Sievwright RH, Wilkinson JJ, O'Neill, HSC, Berry AJ (2017) Thermodynamic controls on element partitioning between
704 titanomagnetite and andesitic–dacitic silicate melts. *Contrib Mineral Petrol* 172(8):62.
- 705 Sisson TW, Grove TL (1993) Experimental investigations of the role of H₂O in calc-alkaline differentiation and subduction
706 zone magmatism. *Contrib Mineral Petrol*, 113(2):143-166.
- 707 Smith JF (1989) Phase Diagrams of Binary Vanadium Alloys, in: Monograph Series on Alloy Phase Diagrams. ASM
708 International, Materials Park, Ohio, p. 251.
- 709 Sossi PA, Halverson GP, Nebel O, Eggins SM (2015) Combined Separation of Cu, Fe and Zn from Rock Matrices and
710 Improved Analytical Protocols for Stable Isotope Determination. *Geostand Geoanalytical Res* 39(2):129-149
- 711 Sossi PA, O'Neill HSC (2017) The effect of bonding environment on iron isotope fractionation between minerals at high
712 temperature. *Geochim Cosmochim Acta*, 196:121-143
- 713 Sossi PA, Moynier F, Chaussidon M, Villeneuve J, Kato C, Gounelle M (2017) Early Solar System irradiation quantified by
714 linked vanadium and beryllium isotope variations in meteorites. *Nature Astronomy*, 1:0055.
- 715 Sutton SR, Karner J, Papike J, Delaney JS, Shearer C, Newville M, Eng P, Rivers M, Dyar MD (2005) Vanadium K edge
716 XANES of synthetic and natural basaltic glasses and application to microscale oxygen barometry. *Geochim*
717 *Cosmochim Acta* 69:2333–2348.
- 718 Thornber CR, Roeder PL, Foster JR (1980) The effect of composition on the ferric-ferrous ratio in basaltic liquids at
719 atmospheric pressure. *Geochim Cosmochim Acta*, 44(3):525-532.
- 720 Toplis MJ, Carroll MR (1995) An experimental study of the influence of oxygen fugacity on Fe-Ti oxide stability, phase
721 relations, and mineral—melt equilibria in ferro-basaltic systems. *J Petrol*, 36(5):1137-1170.
- 722 Turner SP, Foden JD, Morrison RS (1992) Derivation of some A-type magmas by fractionation of basaltic magma: an
723 example from the Padthaway Ridge, South Australia. *Lithos*, 28(2):151-179.
- 724 Toplis MJ, Corgne A (2002) An experimental study of element partitioning between magnetite, clinopyroxene and iron-
725 bearing silicate liquids with particular emphasis on vanadium. *Contrib to Mineral Petrol* 144:22–37.
- 726 Urey HC (1947) The thermodynamic properties of isotopic substances. *J Chem Soc*, 562-581.
- 727 Woodland AB, O'Neill HSC (1997) Thermodynamic data for Fe-bearing phases obtained using noble metal alloys as redox
728 sensors. *Geochim Cosmochim Acta* 61:4359–4366.
- 729 Wu C, Mason T O (1981) Thermopower measurement of cation distributio in magnetite. *J Am Ceram Soc* 64(9):520-522
- 730 Wu F, Qin T, Li X, Liu Y, Huang JH, Wu Z, Huang F (2015) First-principles investigation of vanadium isotope fractionation
731 in solution and during adsorption. *Earth Planet Sci Lett*, 426:216-224.
- 732 Wu F, Qi Y, Yu H, Tain S, Hou Z, Huang F (2016) Vanadium isotope measurement by MC-ICP-MS. *Chem Geol*, 421:17-
733 25.
- 734 Young ED, Tonui E, Manning CE, Schauble EA, Macris CA (2009) Spinel–olivine magnesium isotope thermometry in the
735 mantle and implications for the Mg isotopic composition of Earth. *Earth Planet Sci Lett* 288:524–533

Figure Captions

Fig. 1 Back-scattered electron image of experimental run D1555 (Re-ReO₂). Bright crystals are magnetite, while the darker regions are glass.

Fig. 2 The concentration of **a**) FeO (wt. %) and **b**) V (ppm) measured in the glass by EPMA as a function of $f\text{O}_2$. Error bars on symbols are 1SD

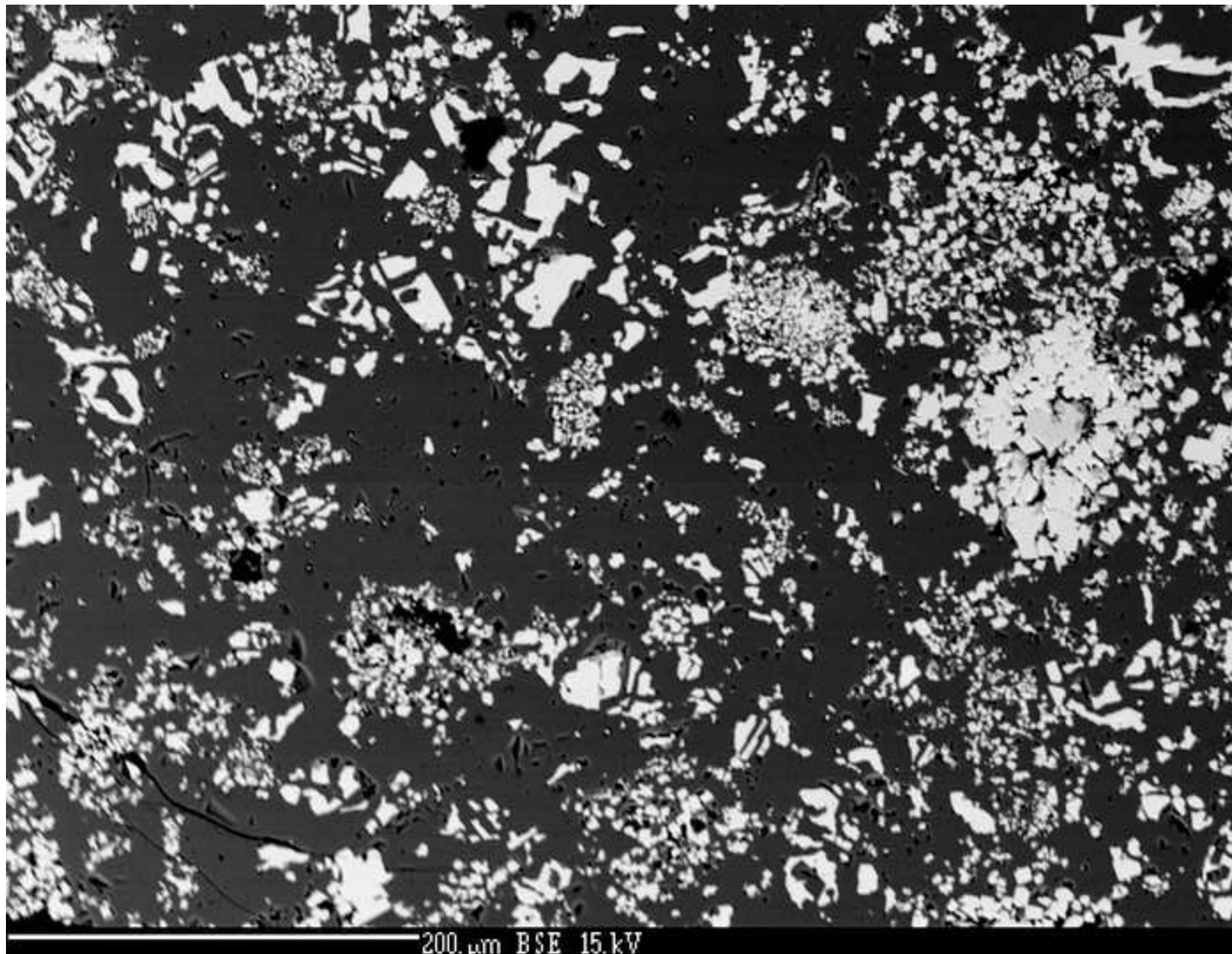
Fig. 3 The control of $\log f\text{O}_2$ (expressed relative to the FMQ buffer, ΔFMQ ; O'Neill, 1987) on the relative proportions of redox-sensitive species for **a**) $\text{Fe}^{2+}/\text{Fe}^{3+}$. Compositions are hydrous haplogranite (orange curve, this work), $(\text{Na,K})_2\text{Si}_3\text{O}_7$ liquids (Knipping et al., 2015) and Mid-Ocean Ridge Basalt, MORB (Berry et al., 2018). Numbers refer to the $\log K^*$ value of reaction 10. **b**) $\text{V}^{3+}/\text{V}^{4+}/\text{V}^{5+}$. The relative abundance of vanadium species is shown by the red line (V^{3+}), green line (V^{4+}) and blue line (V^{5+}) for the hydrous haplogranite composition (this work), calculated from values of the equilibrium constants for reactions 15, 17 and 18. See *Partitioning and redox-dependence of Fe and V*.

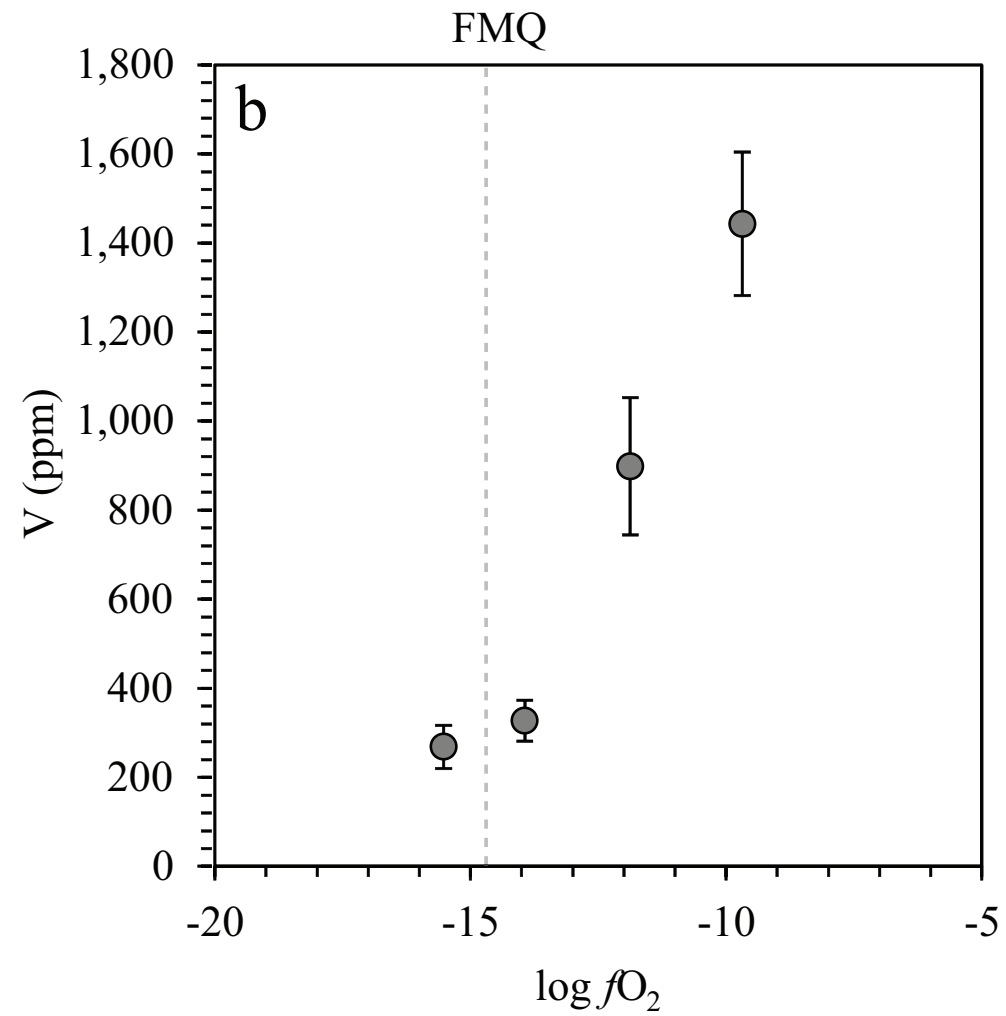
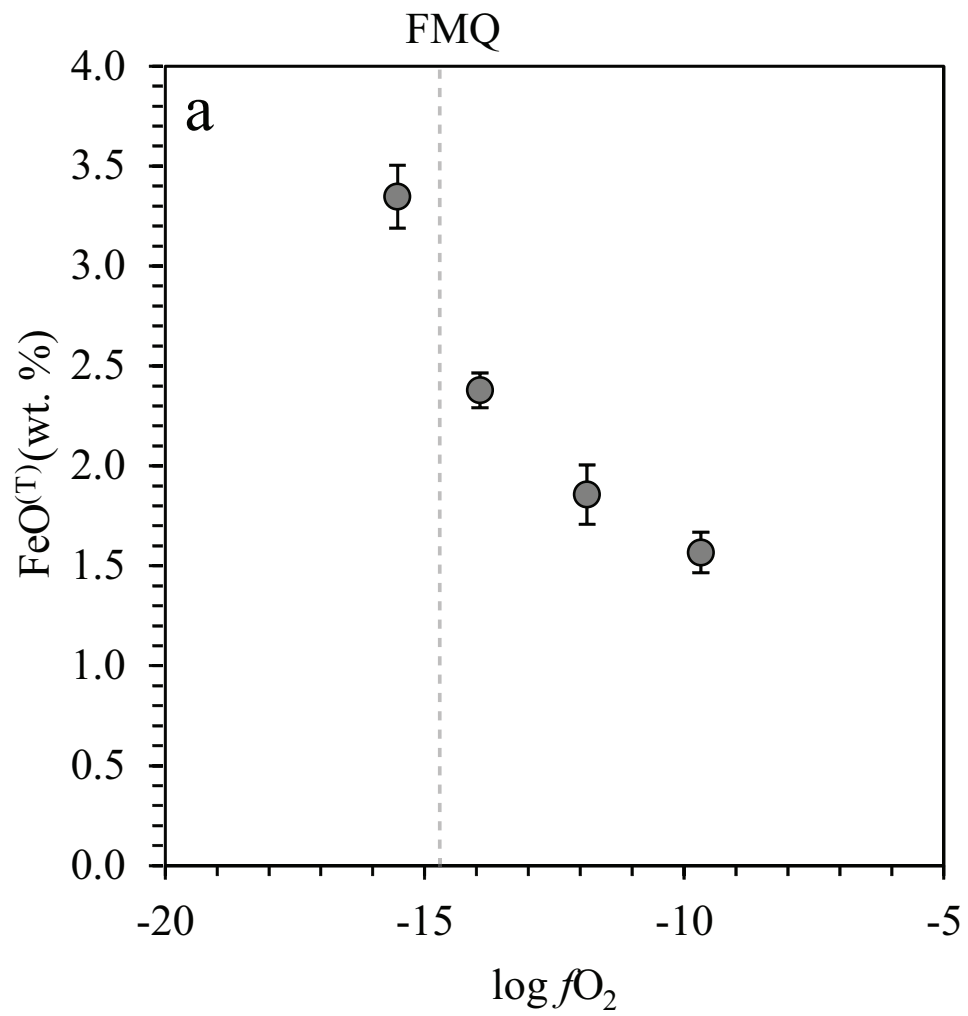
Fig. 4 The change in the logarithm of the bulk partition coefficient of vanadium between magnetite and melt ($\log D_V$) as a function of $\log f\text{O}_2$, relative to the FMQ buffer (ΔFMQ ; O'Neill, 1987). Plotted are datasets for different melt compositions; ferrobasalt at 1068°C, 1 bar (green, Toplis and Corgne, 2002); andesite-dacite at 1070-1120°C, 1 bar (Sievwright et al., 2017), and hydrous haplogranite at 800°C, 5 kb (blue, Arató and Audétat, and red, this work). The slope of the curve is proportional to the relative compatibility of V^{3+} over V^{4+} , see *Partitioning and redox-dependence of Fe and V*.

Fig. 5 Measured vanadium isotope fractionation factor between magnetite and melt and its evolution with $f\text{O}_2$ at 800°C. Fits to the data are *i*) a linear regression (dashed line) and associated 1SD confidence envelope (grey field), which corresponds to eq. 24, and *ii*) calculations based on the bond valence model (solid line). See *Controls on V isotope fractionation*.

Fig. 6 The variation of $\delta^{51}\text{V}_{\text{AA}}$ with V content (expressed as V_2O_3 wt. % on a logarithmic scale) in magnetite and melt. Three models of an evolving ferrobasaltic magma are presented at FMQ-1 (red), FMQ+1 (green) and FMQ+3 (blue). The solid lines denote the composition of the magnetite and the associated magmatic range (red field), whereas the dashed lines show the melt composition. In both cases, crystallisation proceeds from high V_2O_3 /light $\delta^{51}\text{V}$ to low V_2O_3 /heavy $\delta^{51}\text{V}$, with the regions of I-type and A-type denoted, corresponding to crystallisation under oxidising and reducing conditions, respectively. See section 5.2.

Figure 1





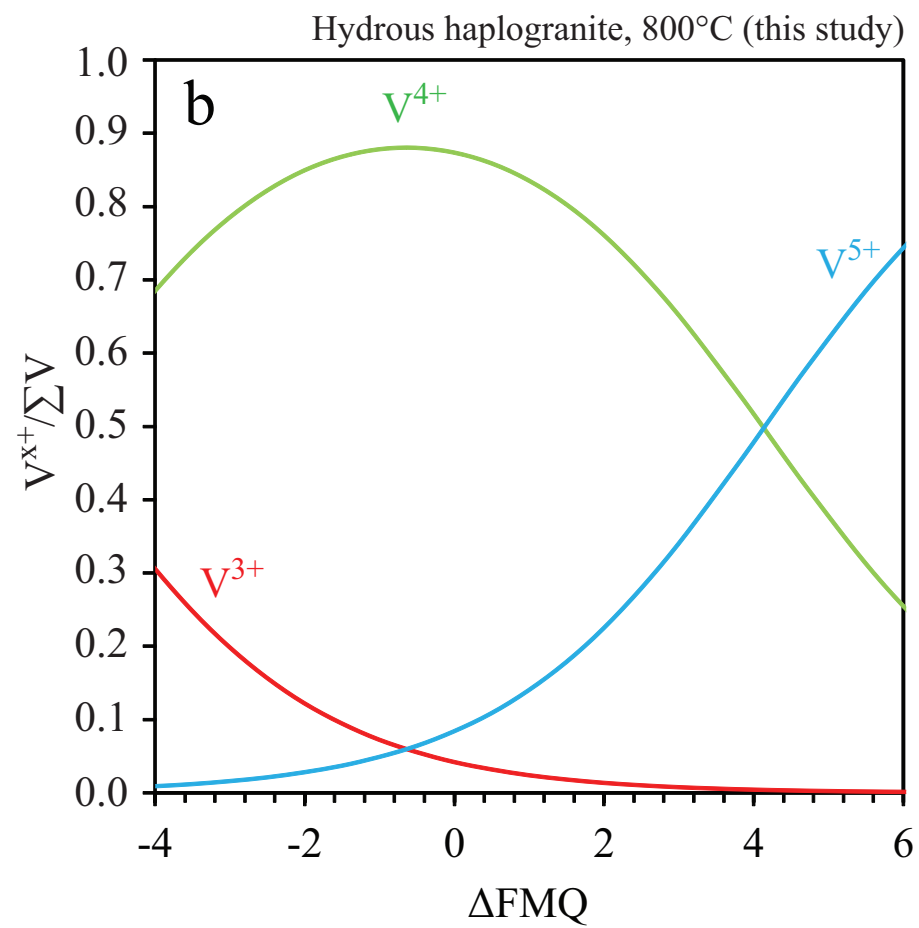
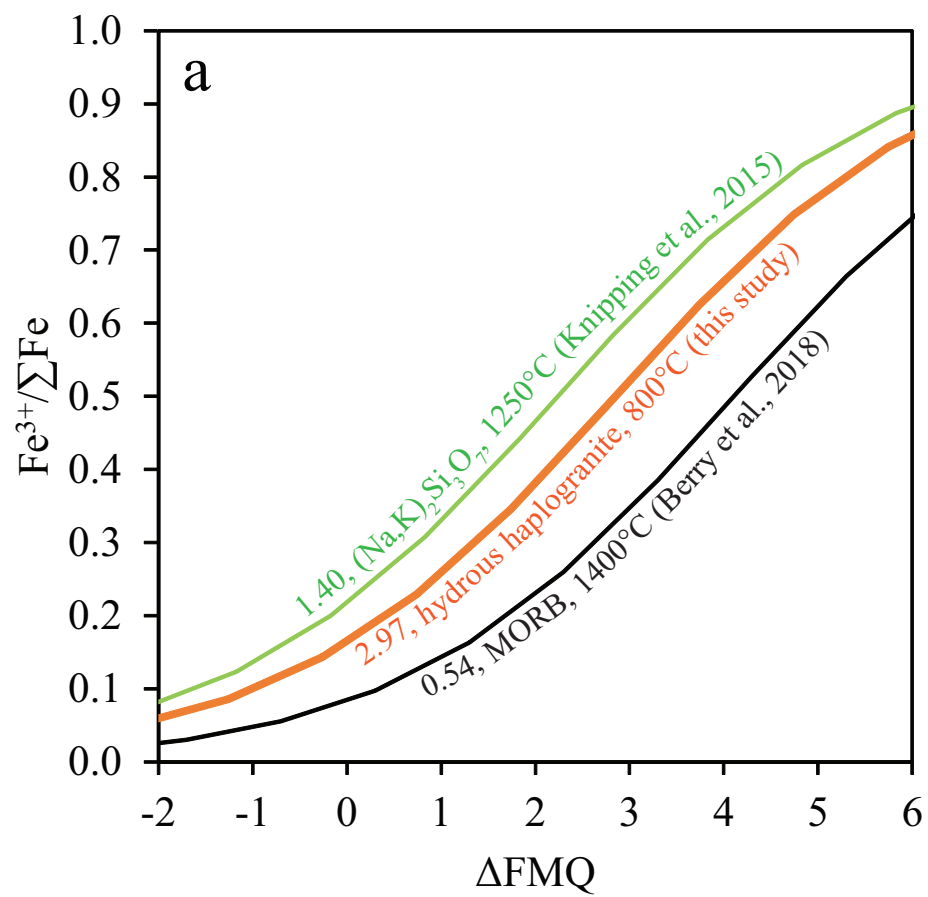
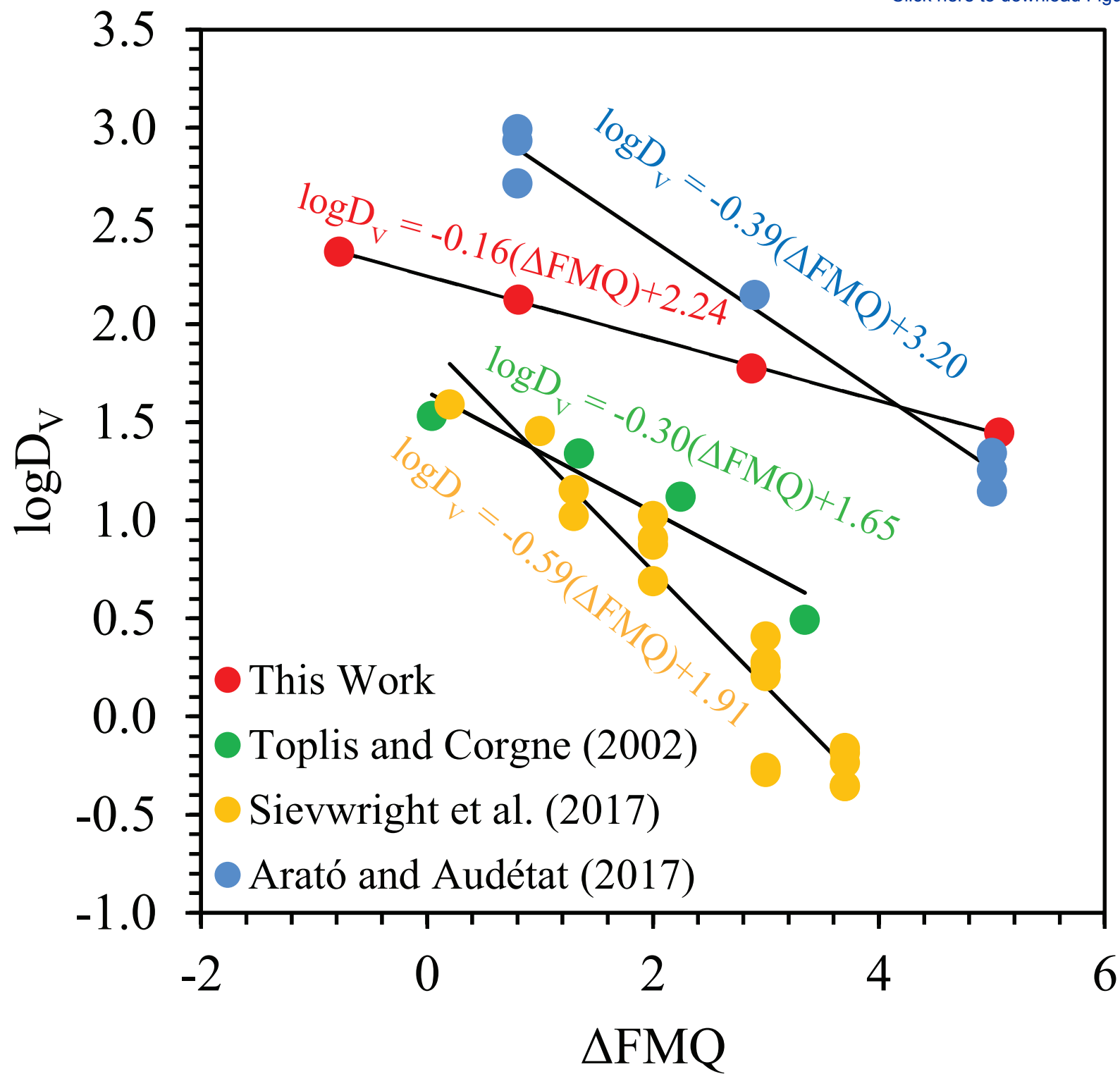
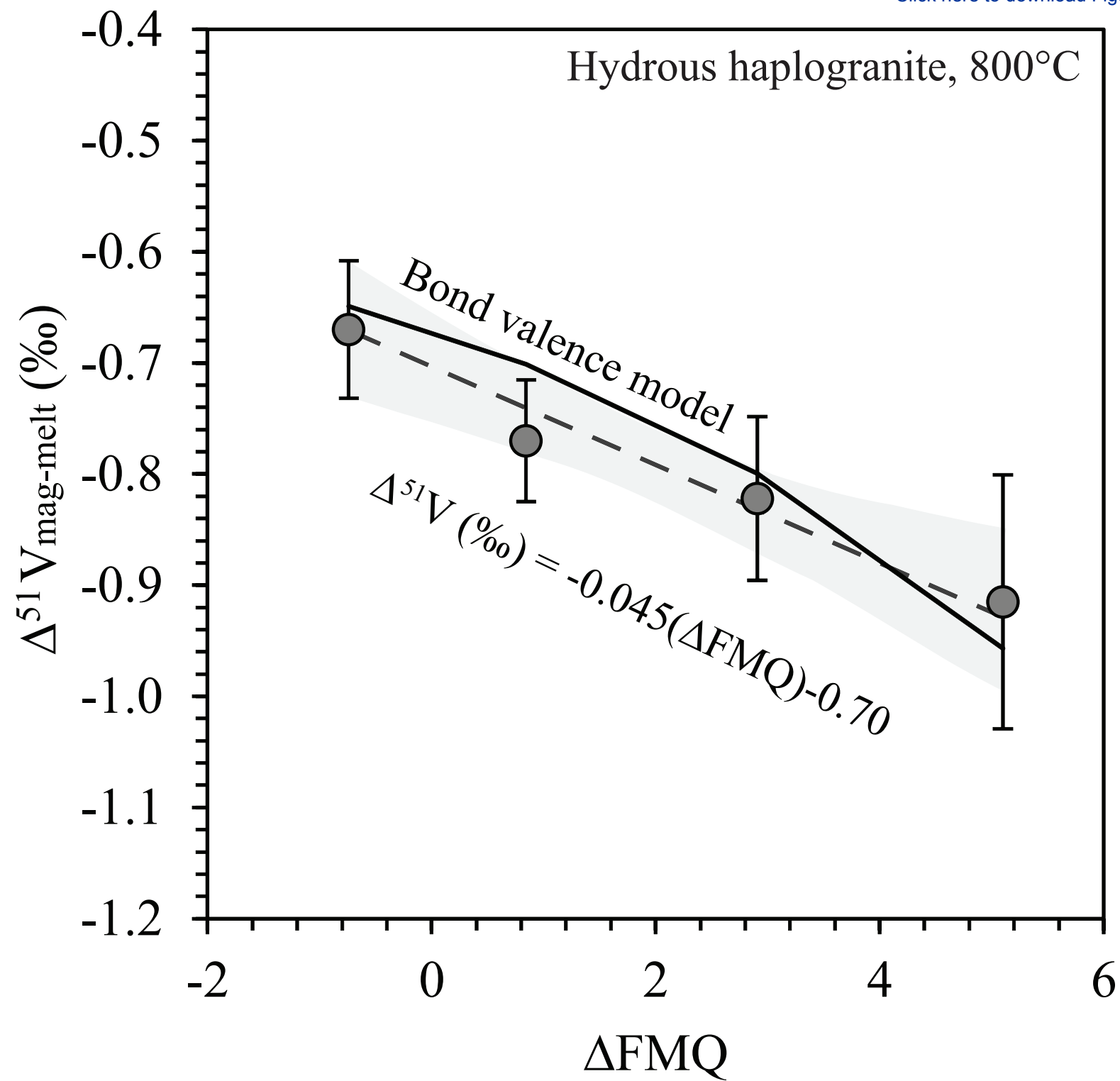


Figure 4





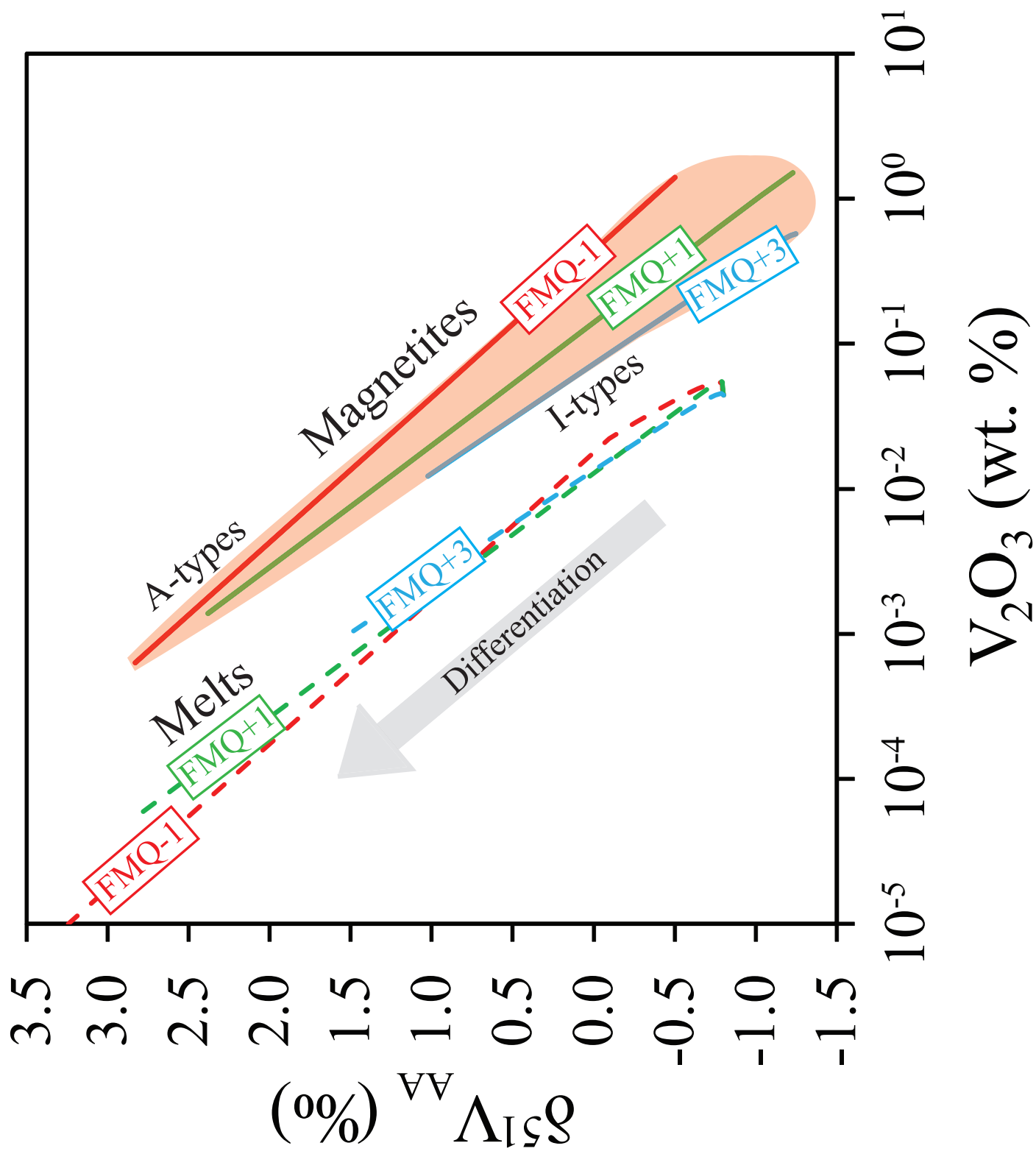


Table 1. Composition of experimental starting mix.

Component	Mass Fraction	Oxide (wt. %)						
		SiO₂	Al₂O₃	Fe₂O₃	Na₂O	K₂O	V₂O₃	H₂O
<i>Piston Cylinder</i>								
PS Haplogranite	0.460	77.64	12.90		4.73	4.74		
Magnetite	0.460			96.66				
Vanadium	0.039						100	
Water	0.041							0.043
<i>1 Atmosphere</i>								
Na-Fe-Silicate	0.980	37		38	23			
Vanadium	0.020						100	

Table 2. Experimental conditions and weights

Press	Name	Inner Capsule	Inner Capsule (g)	Mix (g)	H ₂ O Inner (g)	Outer Ag (g)	Buffer Type	Buffer (g)	H ₂ O Outer (g)	Temperature (°C)	Duration (h)	CO ₂ (sccm)	CO (sccm)
V	D1542	⁷⁵ Ag- ²⁵ Pd	0.2914	0.0686	0.0027	2.9989	HM	0.0547	0.0049	800	72	-	-
V	D1545	⁷⁵ Ag- ²⁵ Pd	0.3069	0.0875	0.0040	2.9852	Co-CoO	0.0516	0.0084	800	72	-	-
A	C4449	⁷⁵ Ag- ²⁵ Pd	0.2216	0.0547	0.0024	3.0045	NNO	0.1572	0.0311	800	336	-	-
V	D1555	⁷⁵ Ag- ²⁵ Pd	0.2530	0.0637	0.0026	2.9788	Re-ReO ₂	0.0982	0.0058	800	168	-	-
C	FMQ-1	Ag	-	-	-	-	CO-CO ₂	-	-	800	163	98	5

Table 3. Cup configuration on Neptune Plus MC-ICP-MS

Cup	L3	L2	L1	C	H1	H2	H3
Resistor	10 ¹¹		10 ¹¹	10 ¹⁰		10 ¹¹	10 ¹¹
Isotope	⁴⁹ Ti		⁵⁰ V	⁵¹ V		⁵² Cr	⁵³ Cr

Table 4. Compositions of experimental phases determined by electron microprobe.

Glasses	<i>n</i>	Oxide (wt. %)								Total
		Na ₂ O	MgO	SiO ₂	Al ₂ O ₃	FeO	K ₂ O	CaO	V ₂ O ₃	
HM	6	2.62	0.01	72.84	12.57	1.57	3.20	0.09	0.21	93.11
±		0.04	0.01	0.90	0.25	0.10	0.13	0.02	0.02	1.13
Re-ReO₂	6	2.58	0.01	71.36	12.94	1.86	3.31	0.09	0.13	92.30
±		0.07	0.02	0.74	0.56	0.15	0.11	0.02	0.02	0.32
NNO	8	3.35	0.04	68.04	13.77	2.38	2.80	0.12	0.05	90.55
±		0.23	0.01	0.49	0.22	0.09	0.09	0.02	0.01	0.65
Co-CoO	5	2.49	0.03	70.96	12.69	3.35	3.28	0.11	0.04	92.97
±		0.06	0.02	0.54	0.08	0.16	0.04	0.02	0.01	0.66
FMQ-1	5	17.68	0.04	49.04	0.17	26.38	0.06	0.25	2.67	96.29
±		0.08	0.02	0.20	0.02	0.25	0.02	0.03	0.03	0.48
<hr/>										
Magnetite										
HM	11		0.12	0.25	0.83	86.23			6.89	94.33
±			0.02	0.32	0.10	0.35			0.27	1.24
Re-ReO₂	8		0.10	0.12	1.02	83.71			7.83	92.78
±			0.03	0.03	0.14	1.04			1.06	0.08
NNO	7		0.10	0.06	0.60	82.14			8.14	91.03
±			0.05	0.07	0.16	0.69			0.65	0.88
Co-CoO	6		0.02	0.08	0.10	84.40			8.39	92.98
±			0.03	0.03	0.03	0.35			0.05	0.32
FMQ-1	6		0.01	0.09	0.00	91.87			0.33	92.31
±			0.01	0.02	0.02	0.62			0.10	0.65
<i>3 Cations/4 Oxygens</i>			<i>Mg²⁺</i>	<i>Si⁴⁺</i>	<i>Al³⁺</i>	<i>Fe²⁺</i>	<i>Fe³⁺</i>		<i>V³⁺</i>	<i>X_{Coul}</i>
HM	11		0.007	0.010	0.037	1.003	1.732		0.210	0.108
Re-ReO₂	8		0.006	0.005	0.046	0.999	1.705		0.240	0.123
NNO	7		0.005	0.002	0.027	0.997	1.719		0.249	0.127
Co-CoO	6		0.006	0.001	0.002	0.995	1.740		0.257	0.129
FMQ-1	6		0.001	0.004	0.000	1.003	1.983		0.010	0.005

Table 5. Vanadium stable isotope compositions of reference materials and standards.

	# dissolutions	# repetitions	$\delta^{51}\text{V}_{\text{AA}}$ (‰)	SD	2SE	Reference
V ₂ O ₃ (BDH)	2	3	-1.17	0.16	0.18	
BDH Solution	N/A	28	-1.13	0.06	0.03	
Column BDH	N/A	3	-1.22	0.12	0.16	
Column AA	N/A	3	-0.12	0.11	0.13	
BCR2	1	2	-1.11	0.04	0.06	This Work
BCR2			-0.95	0.08		Prytulak et al., 2011
BCR2			-0.78	0.04		Wu et al. (2016)
BCR2			-1.03	0.05		Schuth et al. (2017)
BIR-1	3	7	-1.05	0.11	0.08	This Work
BIR-1			-0.94	0.08		Prytulak et al., 2011
BIR-1			-0.92	0.05		Wu et al. (2016)
PCC-1	1	2	-1.02	0.08	0.11	This Work
PCC-1			-1.02	0.04		Prytulak et al., 2011

Table 6. Calculated bulk V content and isotope composition in the experiment and in the magnetite and glass solution fractions, their isotope composition, and the fractionation factor calculated after correcting for contamination.

Experiment	Bulk V ₂ O ₃ (wt. %)	± (SD)	Phase	V (ppm)	f_{mag}	f_{gl}	n	$\delta^{51}\text{V}_{\text{AA}}$ (‰)	± (SD)	$\delta^{51}\text{V}_{\text{AA, corr.}}$ (‰)	Bulk $\delta^{51}\text{V}_{\text{AA}}$ (‰)	$\Delta^{51}\text{V}_{\text{mag-gl}}$ (‰)	± (SD)
HM	3.60	0.31	Magnetite	28523			3	-1.48	0.07	-1.49	-1.46	-0.92	0.11
			Glass	3852	0.053	2	-1.16	0.09	-0.57				
Re-ReO₂	3.98	0.10	Magnetite	29397			3	-1.45	0.06	-1.45	-1.43	-0.82	0.09
			Glass	1954	0.038	2	-1.08	0.07	-0.63				
NNO	3.41	0.16	Magnetite	34197			3	-1.79	0.06	-1.79	-1.73	-0.77	0.08
			Glass	327	0.004	2	-1.09	0.06	-1.02				
Co-CoO	4.22	0.24	Magnetite	25668			3	-1.35	0.06	-1.35	-1.33	-0.67	0.08
			Glass	520	0.014	1	-0.98	-	-0.68				
FMQ-1*	1.82	0.06	Magnetite	2890		0.04	1	-1.35	-	-1.51	-0.95	-0.63	0.09
			Glass	13545		2	-0.88	0.09	-0.88				

* FMQ-1 is a 1 atm experiment

NB: Isotope compositions are quoted following correction for contamination (see *Correction for contamination and open-system behaviour of V in experiments*)

Table 7. Values of equilibrium constants and resulting $\text{Fe}^{2+}/\text{Fe}^{3+}$ and $\text{V}^{3+}/\text{V}^{4+}/\text{V}^{5+}$ ratios in the melt calculated by least-squares fit to the experimental partitioning data. Numbers in brackets refer to 1SD uncertainties. See *Partitioning and redox-dependence of Fe and V*.

	$\text{Log } K^*_{(9)}$	$\text{Log } K^*_{(10)}$	$\text{Log } K^*_{(15)}$	$\text{Log } K^*_{(17)}$	$\text{Log } K^*_{(18)}$	
<i>Global</i>	6.34(30)	2.97(8)	11.09(19)	5.04(12)	2.65(10)	
χ^2	5.48			0.15		
	$\text{Fe}^{3+}/\Sigma\text{Fe}$		$\text{V}^{3+}/\Sigma\text{V}$	$\text{V}^{4+}/\Sigma\text{V}$	$\text{V}^{5+}/\Sigma\text{V}$	$\text{V}^{x+}/\Sigma\text{V}$
<i>Co-CoO</i>	0.12(2)		0.06(2)	0.88(4)	0.06(2)	4.00(1)
<i>Ni-NiO</i>	0.24(3)		0.02(1)	0.85(5)	0.13(3)	4.11(3)
<i>Re-ReO₂</i>	0.52(4)		0.01(0)	0.66(7)	0.34(5)	4.33(5)
<i>HM</i>	0.80(2)		0.00(0)	0.35(9)	0.65(9)	4.65(10)

Table 8. Parameters for calculating the isotope fractionation from the bond valence model. See *Controls on V isotope fractionation*. z = valence, v = co-ordination, s = bond valence, r = bond length, K_f = force constant.

Experiment	Phase	z_v	v_v	s_v	s_o	$r_{v,o}$ (m)	K_f (N/m)	\pm (SD)
HM	Magnetite	3.00	6	0.50	0.50	2.00×10^{-10}	281	56
	Melt	4.65	4.5	1.03	0.80	1.79×10^{-10}	890	178
Re-ReO₂	Magnetite	3.00	6	0.50	0.50	2.00×10^{-10}	281	56
	Melt	4.33	4.5	0.96	0.80	1.83×10^{-10}	815	163
NNO	Magnetite	3.00	6	0.50	0.50	2.00×10^{-10}	281	56
	Melt	4.11	4.5	0.91	0.80	1.85×10^{-10}	749	150
Co-CoO	Magnetite	3.00	6	0.50	0.50	2.00×10^{-10}	281	56
	Melt	4.00	4.5	0.89	0.80	1.87×10^{-10}	715	143